Stochastic Bandgap Optimization for Multiscale Elastic Metamaterials with Manufacturing Imperfections

Minghui Zhang , Qihan Wang , Zhen Luo , Wei Gao

PII: S0020-7403(24)00078-X
DOI: https://doi.org/10.1016/j.ijmecsci.2024.109035
Reference: MS 109035

To appear in: *International Journal of Mechanical Sciences*

Received date: 19 October 2023
Revised date: 9 January 2024
Accepted date: 9 January 2024

Please cite this article as: Minghui Zhang , Qihan Wang , Zhen Luo , Wei Gao , Stochastic Bandgap Optimization for Multiscale Elastic Metamaterials with Manufacturing Imperfections, *International Journal of Mechanical Sciences* (2024), doi: https://doi.org/10.1016/j.ijmecsci.2024.109035

Highlights

- A stochastic bandgap optimization framework for elastic metamaterials is proposed.
- Microscale porosity and uncertainties of elastic metamaterials are considered.
- The desirability function of statistical moments for bandwidths is optimized.
- An adaptively mutation-based particle swarm optimization is developed.

Stochastic Bandgap Optimization for Multiscale Elastic Metamaterials with Manufacturing Imperfections

Minghui Zhang[a], Qihan Wang[a], Zhen Luo[b], Wei Gao[a,*]

[a]Centre for Infrastructure and Safety, School of Civil and Environmental Engineering, The University of New South Wales, Sydney, NSW, 2052, Australia
[b]School of Mechanical and Mechatronic Engineering, The University of Technology Sydney, Sydney, NSW, 2007, Australia

[*]**Corresponding author.** E-mail: w.gao@unsw.edu.au (W. Gao)

Abstract

Bandgaps are endowed to elastic metamaterials (EMMs) attributed to the rationally designed unit cells and extensive works are devoted to bandgap enlargement for improving the applicability of EMMs in multi-disciplinary applications. Nonetheless, most existing optimization frameworks neglect manufacturing imperfections, such as microscale heterogeneity and system uncertainties, which can significantly affect bandgap behaviours. Without properly accounting for these effects, the design may fail to achieve the optimal goal, exhibiting consistently ultra-wide wave attenuation bands in practical EMMs. Herein, in this paper, a stochastic bandgap optimization framework is developed for EMMs involving manufacturing imperfections, aiming at optimizing the first two statistical moments of the normalized bandwidth (NB) simultaneously. To alleviate the large computational costs in approximating statistical moments, a surrogate model is employed to reveal the constitutive relationship between system parameters and NB for the multiscale EMM. Moreover, to solve the optimization problem effectively and efficiently, a high-order mutation strategy is proposed to develop an improved particle swarm optimization (PSO) variant, namely the adaptively high-order mutation-based PSO (AHMPSO). To demonstrate the viability and efficiency of the proposed framework, a numerical investigation is implemented on a 3D EMM, which highlights enlarged bandwidths coupling with an improvement in the robustness of optimum.

Keywords: *Elastic metamaterials, Stochastic optimization, Manufacturing imperfections, Multiscale analysis, Machine learning, Particle swarm optimization*

1. Introduction

Elastic metamaterials (EMMs), consisting of rationally designed periodic unit cells, exhibit a multitude of unprecedented characteristics, which demonstrate significant applicability across diverse fields, such as aerospace, transportation, civil engineering, and the like [1-4]. One of the most captivating characteristics of EMMs is the bandgap, induced by Bragg scattering and local resonance mechanisms [5-9]. With the merits of the bandgap, EMMs can be employed in various applications for wave attenuation, wave guiding, energy trapping, etc. [10,11]. However, one limitation of the developed EMMs is low-frequency bandgaps usually coupled with narrow bandwidths, restricting their real-life applications [12,13]. To alleviate this challenge, extensive works have been devoted to developing parametric [14], structural [15] and topological optimization approaches [16,17] for EMMs aiming at enlarging low-frequency bandgaps [18,19].

With the emergence of 3D printing techniques, metamaterials with complicated topologies can be fabricated [20-23]. Among various additive manufacturing techniques, fused deposition modelling (FDM) is one of the most promising methods, attributed to

the large availability of feedstock materials, fast production, and design flexibility [24-28]. In the FDM process, due to the layer-by-layer feature, a porous is usually found between the deposited filaments once they solidify, denoted as inter-bead porosity [29-31]. An optical image illustrating the cross-section of a FDM part with the inter-bead porosity with a printing angle of 0° is shown in Figure 1.

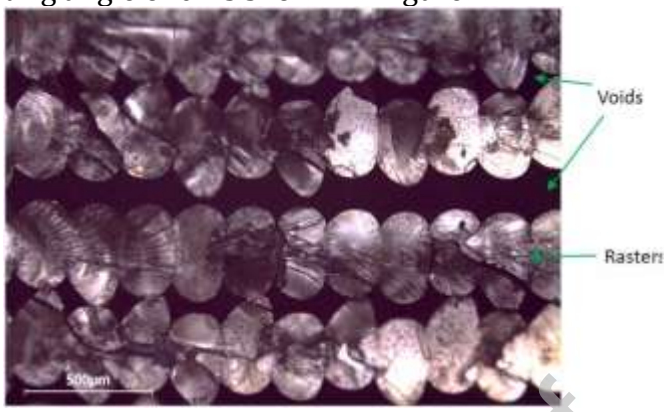

Figure 1: Optical image of the inter-raster voids that were present in 0° raster angle specimens. Scale bar: 500 µm [32].

The inherent manufacturing imperfection can significantly affect the material and mechanical properties of the final products [33-35]. Moreover, another inherent manufacturing imperfection in FDM-fabricated parts is the inevitable system uncertainties, raised from multiple sources, such as measurement, processing, fabrication, environmental factors, etc. [36-38]. Since the bandgap characteristics in EMMs are tightly related to solid constitutes and unit cell architecture, these inevitable manufacturing imperfections significantly affect the corresponding bandgap properties, leading to the scatter of actual system performance in real-life EMMs [39,40]. Therefore, the design candidate from the deterministic optimization may exhibit sub-optimum performance under the presence of uncertainties. In addition, large variations of structural performance also lead to a significant increase in structural life-cycle costs [41,42]. Hence, the optimal goal for bandgap optimization concerns not only the bandwidths but also the consistency of structural performance. To the best of the author's knowledge, there is no existing research on optimizing low-frequency bandwidth for EMMs considering the above-mentioned manufacturing imperfections. Thus, a novel framework is developed herein to fulfil the optimization task for EMMs involving microscale porosity and system uncertainties simultaneously, which are two commonly observed manufacturing imperfections in FDM parts [30,43-45].

With the consideration of randomness in system parameters, bandwidth optimization for multiscale EMMs can be treated as a stochastic optimization problem [46-49]. Instead of solving for a single optimal, two statistical criteria, i.e., the mean and standard deviation of the concerned structural performance, are generally optimized simultaneously [50-52]. To estimate the statistical information for random structural responses, one sampling-based approach with high robustness and flexibility is Monte Carlo simulation (MCS) [53,54]. Specifically, a large number of sampling points for system inputs are generated, which are used to estimate the corresponding structural responses and statistical information of concerned random structural outputs [55]. However, one concern of MCS is that accurate statistical information is generally obtained based on large samples, which may induce high computational costs [56]. To conduct a deterministic bandgap analysis for a multiscale structure, one widely used

method is the multiscale finite element method (FE^2) [57-59]. Nevertheless, a large computational cost is required to conduct a deterministic FE^2 for a multiscale EMM due to a series of cumbersome tasks, including domain discretization, meshing, calculating the homogenized material properties, evaluating physical relationships, and integration of models across scales. Therefore, to conduct the stochastic optimization for multiscale EMMs, one difficulty lies in the large computational burden from approximating the statistical moments, raised by the excessive number of time-consuming deterministic bandgap analysis.

Fortunately, with the blossoming of computer science, a large variety of machine learning techniques have been developed, offering significant benefits in computational efficiency for structural analysis, design, and optimization [60-63]. Among that, a recently developed machine learning algorithm, namely the extended support vector regression (X-SVR), possessing high convergence speed and robustness, has been applied to conduct uncertainty quantification and reliability analysis for a wide range of real-life engineering structures [64-66] involving multiple uncertainty types [36]. Herein, in this research work, to relieve the excessively large computational cost induced by multiscale analysis, the X-SVR is carried out to construct surrogate models, which bridge the underpinned relationship between multiscale structural parameters and normalized bandwidth (NB) for an EMM. With solid mathematical support, the computationally expensive FE^2 model is substituted by the developed surrogate model with an explicit formulation, which extensively relieves the computational burden indued by the multiscale bandgap analysis, providing significant merits on the computational efficiency in stochastic optimization.

In addition to the large computational cost, another challenge in the stochastic optimization problem is to effectively and efficiently solve the optimization problem. Until now, various optimization tools have been developed, from gradient-based mathematical algorithms to non-gradient probabilistic-based search algorithms [67-71]. One nature-inspired metaheuristic probabilistic-based algorithm is particle swarm optimization (PSO). It has attracted considerable attention since it does not require preconditions such as continuity or differentiability of object functions and can be applied to almost all areas of tough optimization problems [72,73]. The algorithm in PSO is that multiple agents (i.e., particles) swarm around the search space, originating from random initial guesses, which communicate the current personal best and share the global best results to explore the global optimum solution. Nevertheless, the use of global best is a double-edged sword, which speeds up convergence, while lacking the ability to explore, leading to premature convergence [72]. To increase the diversity of new solutions, various mutation strategies, generalized as randomization techniques, are introduced into the basic PSO [74-77]. However, different optimization problems may require varied adaptive exploration and exploitation rates during the optimization processes for achieving the global optimum and maintaining high convergence speed. Herein, in this paper, to achieve the balance between exploration and exploitation when solving various optimization problems, a new mutation strategy with high-order functions is proposed to develop a new PSO variant. The newly proposed PSO variant, namely adaptive high-order mutation-based PSO (AHMPSO), is expected to exhibit high convergence speed and exceptional performance in global searching to tackle optimization problems across diverse research fields.

The remainder of the paper is organized as follows. The formulations of the deterministic multiscale bandgap analysis and bandgap optimization are demonstrated

in Section 2.1. In Section 2.2, the formulations for stochastic bandgap optimization and the X-SVR algorithm are introduced. Then, the classic PSO, its variants and the newly developed AHMPSO are presented in Section 3. Subsequently, in Section 4, the stochastic bandwidth optimization framework for EMMs involving manufacturing imperfections is introduced. Then, the computational performance of the proposed AHMPSO and the overall optimization framework are tested, and the results are summarized in Section 5. Finally, some conclusions are presented in Section 6.

2. Preliminary

In Section 2, the methods to conduct the deterministic and stochastic NB optimization for 3D EMMs are discussed in Sections 2.1 and 2.2, respectively. Specifically, the multiscale method to implement the deterministic bandgap analysis is discussed in Section 2.1.1. Then, the formulation of the deterministic bandgap optimization is introduced in Section 2.1.2. Subsequently, the problem formulation of the stochastic bandgap optimization for 3D EMMs involving manufacturing imperfections is demonstrated in Section 2.2.1. Finally, the algorithm for a machine learning method, i.e., X-SVR, is introduced in Section 2.2.2.

2.1. Deterministic Bandgap Optimization for Elastic Metamaterials (EMMs)

2.1.1. Multiscale Bandgap Analysis

A multi-level approach, consisting of two stages of homogenization, is employed to investigate the bandgap characteristics of EMMs involving microscale porosity. In the first stage of homogenization, the equivalent elasticity matrix of the material is derived based on the representative volume element (RVE) homogenization method [57]. Subsequently, the homogenized material properties are applied to the EMM unit cell. A second stage of the homogenization process is then implemented on the EMM unit cell to calculate the bandgap characteristics for the EMM.

2.1.1.1. First Stage Homogenization: Material Homogenization

To derive the equivalent elasticity matrix of the material consisting of micro-porosity, a subscale modelling concept based on representative volume element (RVE) with proper boundary conditions is employed [78]. The concept is established based on the assumption that any material point $\boldsymbol{X} \in \bar{V}$ in the continuum scale is associated with a local RVE whose domain is V with boundary ∂V and the characteristics length of the RVE is much smaller than the length of the continuum scale.

Without loss of generality, considering the RVE is subjected to an external traction $\bar{\boldsymbol{t}}_r$ along its boundary ∂V, the microscopic displacement filed on the RVE boundary, denoted as $\boldsymbol{u}^{\text{micro}}$ can be decomposed into two parts: the mean part $\bar{\boldsymbol{u}}^{\text{micro}}$ and the zero-mean fluctuation part $\tilde{\boldsymbol{u}}^{\text{micro}}$, satisfying

$$u_i^{\text{micro}} = \bar{u}_i^{\text{micro}} + \tilde{u}_i^{\text{micro}} = \bar{\varepsilon}_{ij} x_j + \tilde{u}_i^{\text{micro}}, (i, j = 1, 2, 3), \tag{1}$$

where $\bar{\varepsilon}_{ij}$ represents a volume average of the sub-scale strain and x_j denotes the coordinates of a material point in the Cartesian system. To calculate the effective material properties, periodic boundary conditions are applied over the RVE boundary ∂V, which is decomposed into two parts: a positive part ∂V^+ and a negative part ∂V^- with $\partial V^+ \cup \partial V^- = \partial V, \partial V^+ \cap \partial V^- = \varnothing$ and the associated outward normal $\boldsymbol{n}^+ = -\boldsymbol{n}^-$ at the corresponding points $\boldsymbol{x}^+ \in \partial V^+$ and $\boldsymbol{x}^- \in \partial V^-$, respectively [78]. The applied periodic boundary conditions represent the periodicity of the fluctuations field and anti-periodicity of the traction field on ∂V, specifically,

$$\tilde{\boldsymbol{u}}^{\text{micro}}\left(\boldsymbol{x}^{+}\right)=\tilde{\boldsymbol{u}}^{\text{micro}}\left(\boldsymbol{x}^{-}\right)\ \forall \boldsymbol{x}^{+}\in\partial V^{+}\text{ and matching }\boldsymbol{x}^{-}\in\partial V^{-}, \tag{2}$$

$$\boldsymbol{t}_{r}\left(\boldsymbol{x}^{+}\right)=-\boldsymbol{t}\left(\boldsymbol{x}^{-}\right)\ \forall \boldsymbol{x}^{+}\in\partial V^{+}\text{ and matching }\boldsymbol{x}^{-}\in\partial V^{-}, \tag{3}$$

where $\boldsymbol{t}_r$ denotes the traction field on ∂V. In the absence of body force, the equilibrium state of the RVE is governed by the equilibrium equations:

$$\frac{\partial \sigma_{ij}}{\partial x_j}=0\ \forall \boldsymbol{x}\in V,\ \text{and} \tag{4}$$

$$\sigma_{ij}n_j=\bar{t}_i\ \forall \boldsymbol{x}\in\partial V, \tag{5}$$

where σ_{ij} is the microscopic stress. The mechanical property of the micro-constituents is derived through a constitutive law, i.e., $\sigma_{ij}=\dfrac{\partial W}{\partial \varepsilon_{ij}}$, where ε_{ij} is the microscopic strain. Then, the homogenized stress tensor $\bar{\boldsymbol{\sigma}}$ and homogenized strain tensor $\bar{\boldsymbol{\varepsilon}}$, are defined as the volume average of the sub-scale stress and strain tensors over the RVE,

$$\begin{aligned}\bar{\sigma}_{ij}&=\frac{1}{V}\int_V \sigma_{ij}dV,\ \text{and}\\ \bar{\varepsilon}_{ij}&=\frac{1}{V}\int_V \varepsilon_{ij}dV,\end{aligned} \tag{6}$$

where $\bar{\sigma}_{ij}$ .and $\bar{\varepsilon}_{ij}$ are homogenized components of stress and strain, respectively in the mesoscale. In the case of linear material behavior, the effective moduli component C_{ijkl} can be calculated by applying a suitable strain tensor $\bar{\boldsymbol{\varepsilon}}$ through boundary conditions in Eq. (1) to the RVE [78].

2.1.1.2. Second Stage Homogenization: Bandgap Analysis

The derived material properties C_{ijkl} are applied on the mesoscale EMM unit cell to simulate the elastic wave propagation in the macroscale EMM. The corresponding governing equation is given by [79]

$$\rho\frac{\partial^2 \mathbf{u}_i}{\partial^2 t^2}=\sum_{j=1}^{3}\frac{\partial}{\partial x_j}\left(\sum_{l=1}^{3}\sum_{k=1}^{3}c_{ijkl}\frac{\partial \mathbf{u}_{\mathbf{k}}}{\partial x_l}\right),\left(i=1,2,3\right), \tag{7}$$

where ρ denotes the density of the material; $\mathbf{u}_i$ indicates the displacement vector; t denotes time. Considering an EMM with repeating unit cells, the Floquet-Bloch theorem is employed to solve Eq. (7). The solution can be written as:

$$\mathbf{u}\left(\mathbf{r}\right)=\mathbf{u}_{\mathbf{k}}\left(\mathbf{r}\right)e^{i\left(\mathbf{k}\cdot\mathbf{r}\right)}, \tag{8}$$

where $\mathbf{r}\left(x,y,z\right)$ denotes the position vector and $\mathbf{k}\left(k_x,k_y,k_z\right)$ represents the Bloch wave vector. With the Floquet-Bloch periodicity condition applied in the *x*, *y* and *z* directions, the three components of displacement $\mathbf{u}\left(\mathbf{r}\right)$ can be written as [80]:

$$u\left(x+a,y,z\right)=u\left(x,y,z\right)e^{i\left(k_x\cdot a\right)}, \tag{9}$$

$$u\left(x,y+a,z\right)=u\left(x,y,z\right)e^{i\left(k_y\cdot a\right)}, \tag{10}$$

$$u\left(x,y,z+a\right)=u\left(x,y,z\right)e^{i\left(k_z\cdot a\right)}, \tag{11}$$

where *a* is the lattice constant of the EMM. The wave propagation in EMMs can be obtained by solving the dispersion relation which is an implicit function between the wavevector and the eigenfrequency. By substituting the Eqs. (9)-(11) into Eq.(7), the dispersion relation of a 3D EMM can be obtained by solving the eigenvalue problem:

$$\left(\mathbf{\Gamma}-\boldsymbol{\omega}^2\left(\mathbf{k}\right)\mathbf{M}\right)\mathbf{u}=0, \tag{12}$$

where $\mathbf{\Gamma}\in\Re^{d\times d}$ denotes the stiffness matrix, and $\mathbf{M}\in\Re^{d\times d}$ represents the mass matrix, in which *d* is the degree of freedom (DoF) of the EMM unit cell. By substituting the periodic boundary conditions of Eqs. (9)-(11) into Eq. (12), the solution set $\boldsymbol{\omega}\left(\mathbf{k}\right)^*$ can be written as:

$$\boldsymbol{\omega}\left(\mathbf{k}\right)^*=\left\{\boldsymbol{\omega}_1\left(\mathbf{k}\right),\boldsymbol{\omega}_2\left(\mathbf{k}\right),\ldots,\boldsymbol{\omega}_d\left(\mathbf{k}\right)\right\}. \tag{13}$$

Then, the bandgap characteristics of the EMM are obtained by sweeping the wavevector **k** along the boundary of the first irreducible Brillouin zone [81]. The complete bandgap is identified, which has no eigenfrequency falling into the frequency range along the whole **k**-path. Since the low-frequency wave attenuation performance is mostly concerned, in this research, the structural optimization focuses on the investigation of the 1st bandgap, which is characterized by two quantities, i.e., the starting frequency (f_{s}) and the cut-off frequency (f_{c}). The 1st bandgap is identified by finding the lowest $p_{\min}$, satisfying $\min\left(\boldsymbol{\omega}_{p_{\min}+1}\left(\mathbf{k}\right)\right)-\max\left(\boldsymbol{\omega}_{p_{\min}}\left(\mathbf{k}\right)\right)>0$. Then, the concerned f_{s} and f_{c} are calculated as:

$$f_{\mathrm{s}}=\frac{\max\left(\boldsymbol{\omega}_{p_{\min}}\left(\mathbf{k}\right)\right)}{2\pi}, \tag{14}$$

$$f_{\mathrm{c}}=\frac{\min\left(\boldsymbol{\omega}_{p_{\min}+1}\left(\mathbf{k}\right)\right)}{2\pi}. \tag{15}$$

Another structural response, i.e., NB, assessing the width of the bandgap, is calculated based on the formulation: $\Delta f=2\left(f_{\mathrm{c}}-f_{\mathrm{s}}\right)/\left(f_{\mathrm{c}}+f_{\mathrm{s}}\right)\times100\%$, which is the concerned structural response in this work.

2.1.2. Deterministic Multiscale Bandgap Optimization

The deterministic multiscale bandwidth optimization problem for EMMs is formulated as

$$\begin{cases}\max\limits_{\mathbf{d}} \ \Delta f\left(\mathbf{d}\right)\\ s.t. \ \ \mathbf{d}_{\mathrm{L}}\le\mathbf{d}\le\mathbf{d}_{\mathrm{U}}\end{cases}, \tag{16}$$

where $\Delta f\left(\mathbf{d}\right)$ denotes the NB for an EMM considering microscale porosity, which is the objective function in the deterministic bandgap optimization problem; $\mathbf{d}=\left[d_1,d_2,\ldots,d_{\bar{q}}\right]\in\Re^{\bar{q}}$ represents a vector containing all design variables; $\mathbf{d}_{\mathrm{L}}\in\Re^{\bar{q}}$ and $\mathbf{d}_{\mathrm{U}}\in\Re^{\bar{q}}$ collect the lower and upper bound limits for all design variables, respectively. By solving the optimization problem, the optimum values for design variables are calculated for an EMM considering microscale porosity.

2.2. Stochastic Bandgap Optimization for Elastic Metamaterials (EMMs)

2.2.1. Problem Formulations in Stochastic Bandgap Optimization

Accumulative experiences from industrial applications have revealed that inherent system uncertainties are mandatory to be properly considered in structural optimization to achieve desired structural properties in the fabricated parts [64]. Hence, to effectively enlarge low-frequency NB for practical EMMs involving microscale porosities and system uncertainties, a stochastic multiscale optimization framework for EMMs is developed.

Without loss of generality, let $\boldsymbol{\tau}^{\mathrm{R}} \in \Re^{\bar{p}}$ denotes a $\bar{p}$-dimensional random vector, which collects all random systematic input parameters τ_{ℓ}^{R}, for $\ell = 1, 2, \ldots, \bar{p}$ in a probability space $(\boldsymbol{\Omega}, \boldsymbol{\Lambda}, \mathbf{P})$. The governing equation of the random dispersion relation for EMMs is expressed as:

$$\begin{cases} \left(\boldsymbol{\Gamma}\left(\boldsymbol{\tau}^{\mathrm{R}}\right) - \left(\boldsymbol{\omega}^{\mathrm{R}}\left(\mathbf{k}\right)\right)^{2} \mathbf{M}\left(\boldsymbol{\tau}^{\mathrm{R}}\right)\right)\mathbf{u}^{\mathrm{R}} = 0 \\ \boldsymbol{\tau}^{\mathrm{R}} \in \boldsymbol{\Omega} := \left\{ \boldsymbol{\tau}^{\mathrm{R}} \in \Re^{\bar{p}} \mid \tau_{\ell}^{\mathrm{R}} \sim f_{\tau_{\ell}^{\mathrm{R}}}^{\mathrm{D}}\left(x\right), \text{ for } \ell = 1, 2, \ldots, \bar{p} \right\} \end{cases}, \tag{17}$$

where $\boldsymbol{\Gamma}\left(\boldsymbol{\tau}^{\mathrm{R}}\right) \in \Re^{d \times d}$ and $\mathbf{M}\left(\boldsymbol{\tau}^{\mathrm{R}}\right) \in \Re^{d \times d}$ indicate the random stiffness matrix and mass matrix, respectively, which are functions of the random vector $\boldsymbol{\tau}^{\mathrm{R}}$; $\Re$ indicates a real number; $\mathbf{u}^{\mathrm{R}}$ denotes the random displacement vector; $\boldsymbol{\omega}^{\mathrm{R}}(\cdot) \in \Re^{d}$ represents a random vector collecting eigenfrequencies of the system; $f_{\tau_{\ell}^{\mathrm{R}}}^{\mathrm{D}}\left(x\right)$ is the probability density function (PDF) for the ℓth random variable τ_{ℓ}^{R}. With the introduction of system uncertainties into the EMM, the concerned structural response, i.e., NB also possesses the feature of randomness, denoted as Δf^{R}. In the structural optimization problem with stochastic parameters, a straightforward method to define the optimality condition is based on the first two statistical moments, i.e., the mean value $\mu\left(\triangle f\left(\bullet\right)\right)$ and standard deviation $\sigma\left(\triangle f\left(\bullet\right)\right)$ of the concerned structural response. For achieving the optimal goal in EMM, exhibiting large bandwidth and high robustness at optimality, the mathematical formulation for the multi-objective optimization problem is expressed as

$$\begin{cases} \max\limits_{\mathbf{d}} \mu\left(\triangle f\left(\mathbf{d}, \boldsymbol{\tau}^{\mathrm{R}}\right)\right) \\ \min\limits_{\mathbf{d}} \sigma\left(\triangle f\left(\mathbf{d}, \boldsymbol{\tau}^{\mathrm{R}}\right)\right) \\ st. \quad \mathbf{d}_{\mathrm{L}} \le \mathbf{d} \le \mathbf{d}_{\mathrm{U}} \end{cases} \tag{18}$$

Under the optimization, the design is expected to demonstrate a large bandwidth, which improves the applicability of EMMs in multi-disciplinary applications. Meanwhile, the minimization of standard deviation ensures the system is less sensitive to system uncertainties, giving rise to the need for a more robust design.

In multi-objective optimization problems, the two design criteria may conflict with each other, which means that a trade-off between the two objectives is generally required to be made. Instead of solving for the single optimal, Pareto optimality is an alternative method to define a vector optimum. Specifically, for each element in this set, none of the objective functions can be further improved without worsening the remaining objective functions. A straightforward approach to Pareto optimal solutions is through the linear combination method. The optimization problem can then be formulated in terms of a desirability function f_{d}. The corresponding mathematical formulation for the bandgap optimization problem is expressed as:

$$\begin{cases} \min\limits_{\mathbf{d}} \quad f_{\mathrm{d}} = w_{\mathrm{s}} \left(\sigma\left(\triangle f\left(\mathbf{d}, \boldsymbol{\tau}^{\mathrm{R}}\right)\right)\right) \Big/ \sigma^{*} + \left(1 - w_{\mathrm{s}}\right)\left(-\mu\left(\triangle f\left(\mathbf{d}, \boldsymbol{\tau}^{\mathrm{R}}\right)\right)\right) \Big/ \mu^{*} \\ s.t. \quad \mathbf{d}_{\mathrm{L}} \le \mathbf{d} \le \mathbf{d}_{\mathrm{U}} \end{cases}, \tag{19}$$

where $0 < w_s < 1$ is the factor weighting the two objective functions; μ^* and σ^* are normalization factors. The problem can be converted into a mean value maximization problem when w_s = 0 and a standard deviation minimization problem when w_s = 1.

To tackle the stochastic optimization problem, one essential task is to estimate the mean and standard deviation for the concerned structural response. One sampling-based approach with high robustness is through MCS. However, one concern is the substantial computational cost induced by the numerous evaluations of multiscale bandgap analysis, since the deterministic FE^2 is already time-consuming due to a series of cumbersome tasks, including domain discretization, meshing, evaluation of the constitutive relationships and integration of physical models across scales.

2.2.2. Surrogate Model Construction by Extended Support Vector Regression (X-SVR)

To relieve the large computational cost arising from the numerous evaluations of multiscale bandgap analysis for EMMs, a machine learning algorithm, namely the extended support vector regression (X-SVR) is employed. Through solid mathematical support, a surrogate model is generated, bridging the relationship between multiscale system parameters and NB for an EMM by an explicit formulation. In the X-SVR, through applying kernel mapping strategy, the linear X-SVR can be extended to the nonlinear X-SVR for solving complex engineering problems. For a given training dataset input vector $\mathbf{x} = \left[\mathbf{x}_1, \mathbf{x}_2, \ldots, \mathbf{x}_m\right]^{\mathrm{T}} \in \Re^{m \times n}$ and output vector $\mathbf{y} = \left[y_1, y_2, \ldots, y_m\right]^{\mathrm{T}} \in \Re^m$, in which m represents the number of training samples and $n = \bar{p} + \bar{q}$ denotes the dimension of the inputs $\mathbf{x}$, the developed surrogate model is formulated as,

$$\hat{f}\left(\mathbf{x}\right) = \boldsymbol{\kappa}\left(\mathbf{x}\right)\mathbf{w} + \delta, \tag{20}$$

where $\mathbf{w} = \left[w_1, w_2, \ldots, w_n\right]^{\mathrm{T}} \in \Re^n$ and $\delta \in \Re$ represent the normal and bias of the targeted hyperplanes respectively; $\boldsymbol{\kappa}(\mathbf{x})$ represents the kernelized training input matrix. The nonlinear X-SVR surrogate model can be obtained by solving the optimization problem that is expressed as:

$$\min_{\mathbf{p},\mathbf{q},\delta,\xi,\xi^*} : \left(\left\|\mathbf{p}\right\|_2^2 + \left\|\mathbf{q}\right\|_2^2\right) + \lambda \mathbf{e}_n^{\mathrm{T}}\left(\mathbf{p} + \mathbf{q}\right) + \frac{C}{2}\left(\xi^{\mathrm{T}}\xi + \xi^{*\mathrm{T}}\xi^*\right) \tag{21}$$

$$s.t. \begin{cases} \boldsymbol{\kappa}\left(\mathbf{x}\right)\left(\mathbf{p} - \mathbf{q}\right) + \delta\mathbf{e}_m - \mathbf{y} \le \varepsilon\mathbf{e}_m + \xi \\ \mathbf{y} - \boldsymbol{\kappa}\left(\mathbf{x}\right)\left(\mathbf{p} - \mathbf{q}\right) - \delta\mathbf{e}_m \le \varepsilon\mathbf{e}_m + \xi^* \\ \mathbf{p}, \mathbf{q} \ge \mathbf{0}_n,\ \xi,\ \xi^* \ge \mathbf{0}_m \end{cases}, \tag{22}$$

where $\lambda \in \Re^+$ indicates a tuning parameter for balancing the performance of regression and feature selection; ε denotes the soft margin; $\xi \in \Re^m$ and $\xi^* \in \Re^m$ represent two non-negative vectors collecting slack variables; $\mathbf{e}_n = \left[1, 1, \ldots, 1\right]^{\mathrm{T}} \in \Re^n$ and $\mathbf{0}_n = \left[0, 0, \ldots, 0\right]^{\mathrm{T}} \in \Re^n$ represent the ones vector and the zeros vector, respectively; $\mathbf{p}, \mathbf{q} \in \Re^n$ are two negative variables [82]; C denotes a penalty constant. Notably, for kernelized input matrix, the dimension of features equals the number of training sets, i.e., $n = m$. Subsequently, the optimization problem is simplified as:

$$\min_{\hat{\mathbf{z}},\delta} : \frac{1}{2}\left(\hat{\mathbf{z}}^{\mathrm{T}}\hat{\mathbf{C}}\hat{\mathbf{z}} + \delta^2\right) + \lambda\hat{\mathbf{a}}^{\mathrm{T}}\hat{\mathbf{z}} \tag{23}$$

$$s.t.\ \left(\hat{\mathbf{A}}+\mathbf{I}_{4m}\right)\hat{\mathbf{z}}+\left(\varepsilon\mathbf{I}_{4m}+\delta\hat{\mathbf{G}}\right)\hat{\mathbf{b}}+\hat{\mathbf{d}}\geq\mathbf{0}_{4m}, \quad (24)$$

where $\mathbf{I}_{4m}\in\Re^{4m\times 4m}$ indicates the identify matrix $\hat{\mathbf{C}},\hat{\mathbf{G}}$ and $\hat{\mathbf{A}}\in\Re^{4m\times 4m}$ are defined as:

$$\hat{\mathbf{C}}=\begin{bmatrix}\mathbf{I}_{2m} & \\ & C\mathbf{I}_{2m}\end{bmatrix},\ \hat{\mathbf{G}}=\begin{bmatrix}\mathbf{0}_{2m\times 2m} & \mathbf{0}_{2m\times m} & \mathbf{0}_{2m\times m}\\ \mathbf{0}_{m\times 2m} & \mathbf{I}_{m} & \mathbf{0}_{m\times m}\\ \mathbf{0}_{m\times 2m} & \mathbf{0}_{m\times m} & -\mathbf{I}_{m}\end{bmatrix},\ \hat{\mathbf{A}}=\begin{bmatrix}\mathbf{0}_{2m\times m} & \mathbf{0}_{2m\times m} & \mathbf{0}_{2m\times 2m}\\ -\boldsymbol{\kappa}(\mathbf{x}) & \boldsymbol{\kappa}(\mathbf{x}) & \mathbf{0}_{m\times 2m}\\ \boldsymbol{\kappa}(\mathbf{x}) & -\boldsymbol{\kappa}(\mathbf{x}) & \mathbf{0}_{m\times 2m}\end{bmatrix}, \quad (25)$$

and the kernelized vectors $\hat{\mathbf{a}},\hat{\mathbf{b}},\hat{\mathbf{d}}$ and $\hat{\mathbf{z}}\in\Re^{4m}$ are defined as:

$$\hat{\mathbf{a}}=\begin{bmatrix}\mathbf{e}_{2m}\\ \mathbf{0}_{2m}\end{bmatrix},\ \hat{\mathbf{b}}=\begin{bmatrix}\mathbf{0}_{2m}\\ \mathbf{e}_{2m}\end{bmatrix},\ \hat{\mathbf{d}}=\begin{bmatrix}\mathbf{0}_{2m}\\ \mathbf{y}\\ -\mathbf{y}\end{bmatrix},\ \hat{\mathbf{z}}=\begin{bmatrix}\mathbf{p}\\ \mathbf{q}\\ \boldsymbol{\xi}\\ \boldsymbol{\xi}^{*}\end{bmatrix}. \quad (26)$$

Then, the kernelized X-SVR is solved with the introduction of a non-negative Lagrange multiplier $\boldsymbol{\varphi}\in\Re^{4m}$. Through the way for solving a quadratic programming (QP) problem, the optimization problem can further be formulated as:

$$\min_{\boldsymbol{\varphi}}:\frac{1}{2}\boldsymbol{\varphi}^{\mathrm{T}}\mathbf{Q}\boldsymbol{\varphi}-\mathbf{m}^{\mathrm{T}}\boldsymbol{\varphi} \quad (27)$$

$$s.t.\ \boldsymbol{\varphi}\geq\mathbf{0}_{4m}, \quad (28)$$

where $\mathbf{Q}\in\Re^{4m\times 4m}$ and $\mathbf{m}\in\Re^{4m}$ are defined as:

$$\mathbf{Q}=\left(\hat{\mathbf{A}}+\mathbf{I}_{4m}\right)\hat{\mathbf{C}}^{-1}\left(\hat{\mathbf{A}}+\mathbf{I}_{4m}\right)^{\mathrm{T}}+\hat{\mathbf{G}}\hat{\mathbf{b}}\hat{\mathbf{b}}^{\mathrm{T}}\hat{\mathbf{G}}, \quad (29)$$

$$\mathbf{m}=\lambda\left(\hat{\mathbf{A}}+\mathbf{I}_{4m}\right)\hat{\mathbf{C}}^{-1}\hat{\mathbf{a}}-\varepsilon\hat{\mathbf{b}}-\hat{\mathbf{d}}. \quad (30)$$

Let $\boldsymbol{\varphi}^{*}$ be the solution of optimization problems in Eqs. (27) and (28), then the variables $\hat{\mathbf{z}}$ and δ can be determined as:

$$\hat{\mathbf{z}}=\hat{\mathbf{C}}^{-1}\left[\left(\hat{\mathbf{A}}+\mathbf{I}_{4m}\right)^{\mathrm{T}}\boldsymbol{\varphi}^{*}-\lambda\hat{\mathbf{a}}\right], \quad (31)$$

$$\delta=\hat{\mathbf{b}}^{\mathrm{T}}\hat{\mathbf{G}}\boldsymbol{\varphi}^{*}. \quad (32)$$

Then, the nonlinear regression function can be expressed as:

$$\hat{f}\left(\mathbf{X}\right)=\left(\mathbf{p}-\mathbf{q}\right)^{\mathrm{T}}\boldsymbol{\kappa}\left(\mathbf{X}\right)+\hat{\mathbf{b}}^{\mathrm{T}}\hat{\mathbf{G}}\boldsymbol{\varphi}^{*}. \quad (33)$$

The coefficient $\mathbf{p}$ and $\mathbf{q}$ can be obtained as:

$$\mathbf{p}=\hat{\mathbf{z}}(1:m), \quad (34)$$

$$\mathbf{q}=\hat{\mathbf{z}}(m+1:2m). \quad (35)$$

With the developed surrogate model, the bandgap for EMMs with microscale porosity can be estimated based on an explicit formulation, instead of running the time-consuming FE^{2}. Consequently, the required computational resources to approximate the first two statistical moments are significantly relieved, offering extensive merits in computational efficiency for implementing the stochastic optimization for multiscale EMMs.

3. Particle Swarm Optimization (PSO)

In this Section, the algorithms of the PSO to implement the stochastic optimization for 3D EMMs are introduced. Specifically, the classical PSO and its variants are

discussed in Section 3.1. Then, the algorithm for the newly developed AHMPSO is introduced in Section 3.2.

3.1. Classical Particle Swarm Optimization (PSO) and its Variants

In the basic PSO, the algorithm starts with a population of particles randomly initialized in the search space, in which each particle denotes a potential solution. The position and velocity of the Lth particle are represented by two vectors, i.e., $\mathbf{p}_L = \left[p_{L1}, p_{L2}, \ldots, p_{L\bar{q}} \right]^{\mathrm{T}} \in \Re^{\bar{q}}$ and $\mathbf{v}_L = \left[v_{L1}, v_{L2}, \ldots, v_{L\bar{q}} \right]^{\mathrm{T}} \in \Re^{\bar{q}}$, respectively. The particles update their position based on their personal best and global best encountered so far, which are expressed as [83]

$$\mathbf{v}_L(K+1) = w\mathbf{v}_L(K) + c_1\mathbf{r}_1 \circ \left(\mathbf{p}_L^{\mathrm{Pb}} - \mathbf{p}_L(K)\right) + c_2\mathbf{r}_2 \circ \left(\mathbf{p}^{\mathrm{Gb}} - \mathbf{p}_L(K)\right), \tag{36}$$

$$\mathbf{p}_L(K+1) = \mathbf{p}_L(K) + \mathbf{v}_L(K+1), \tag{37}$$

where K represents the iteration number; $\mathbf{v}_L(K)$ and $\mathbf{p}_L(K)$ denote the velocity and position vectors of the Lth particle at the Kth iteration, respectively; $\mathbf{p}_L^{\mathrm{Pb}}$ indicates the best position explored by the Lth particle until the Kth iteration; $\mathbf{p}^{\mathrm{Gb}}$ denotes the global best position visited by the whole particles until Kth iteration; w denotes the inertia weight controlling the influence of the previous velocity on the current one; c_1 and c_2 represent cognitive parameter and social parameter respectively; $\mathbf{r}_1^{\mathrm{T}} \in \Re^{\bar{q}}$ and $\mathbf{r}_2^{\mathrm{T}} \in \Re^{\bar{q}}$ indicate two random vectors with values that are uniformly distributed in the interval [0, 1]; the symbol $\circ$ represents the Hadamard product.

Balancing exploration and exploitation for improving the global searching ability is always an important task in the optimization algorithm. A PSO variant with linearly decreasing inertia weight and time-varying acceleration coefficient (LPSO-TVAC) is proposed [84]. The detailed algorithm of it is shown in *Appendix A*. Besides, another PSO variant, namely a low-discrepancy sequence initialized particle swarm optimization algorithm with high-order nonlinear time-varying inertia weight (LHNPSO) is proposed by Yang et al. [85]. Three control parameters α, β and γ are introduced to adaptively update the inertia weight and acceleration coefficients. The formulations for updating $w(K), c_1(K)$ and $c_2(K)$ are introduced in *Appendix B*.

3.2. Adaptively High-order Mutation-based Particle Swarm Optimization (AHMPSO)

Though numerous improved PSO algorithms have been developed and applied in many research areas, solving optimization problems with extraordinary performance in global searching and rapid convergence speed is always an important task. Besides using adaptive inertia weight and acceleration coefficients for improving global searching capability, mutation strategies can be introduced into the PSO algorithm, offering significant merit in enhancing global exploration. However, mutation is a double-edged sword, which improves global exploration while slowing down the convergence. Adaptive mutation strategies, generating varied rates of exploration during the optimization process, have been demonstrated to improve global searching ability and maintain a high convergence speed. Some strategies aim at achieving a high exploration rate at the early stage for thoroughly searching the whole design space and a gradually increased exploitation rate at the later stage for concentrating on the best design areas [86]. However, for the problems with numerous local optima, the low exploration rate at the later stage hinders the capability to escape the local optima, which may lead to premature convergence. Hence, it is imperative to propose a mutation strategy, which can designate the exploration and exploitation rates during

the whole optimization process to effectively address multiple optimization problems across diverse fields.

Herein, in this research, an adaptively high-order mutation-based strategy is developed and introduced into the PSO. Specifically, two high-order functions, i.e., $\boldsymbol{\eta}$ and $\mathbf{T}$ are developed and introduced into the formulations for updating velocity and position vectors, which are expressed as

$$\mathbf{v}_L(K+1) = w(K)\mathbf{v}_L(K) + c_1(K)\mathbf{r}_1 \circ \left(\mathbf{p}_L^{\mathrm{Pb}} - \mathbf{p}_L(K)\right) + c_2(K)\mathbf{r}_2 \circ \left(\mathbf{p}_L^{\mathrm{Gb}} - \mathbf{p}_L(K)\right) + \boldsymbol{\eta}, \tag{38}$$

$$\mathbf{p}_L(K+1) = \mathbf{T} \circ \mathbf{p}_L(K) + \mathbf{v}_L(K+1), \tag{39}$$

in which $\boldsymbol{\eta}$ and $\mathbf{T}$ are expressed as

$$\boldsymbol{\eta}(K) = \left(p_{1c}\left(\frac{K}{K_{\max}}\right)^{\hbar} \mathbf{r}_3 \right) \circ (\mathbf{d}_{\mathrm{U}} - \mathbf{d}_{\mathrm{L}}), \tag{40}$$

$$\mathbf{T}(K) = \left(\mathbf{J}_{\bar{p}} - p_{2c}\left(\frac{K}{K_{\max}}\right)^{\phi} \mathbf{r}_4 \right), \tag{41}$$

where $\mathbf{r}_3^{\mathrm{T}} \in \Re^{\bar{q}}$ is a random vector with values following normal distribution; $\mathbf{r}_4^{\mathrm{T}} \in \Re^{\bar{q}}$ is a random vector with values in the interval [-1, 1] following uniform distribution; $\hbar, \phi, p_{1c}$ and p_{2c} are four parameters and $\mathbf{J}_{\bar{p}} \in \Re^{\bar{p}}$ is a vector to control the rates of exploration and exploitation during the whole optimization process; $w(K), c_1(K)$ and $c_2(K)$ are updated based on formulations in Appendix B. The high-order functions offer merits in adaptively controlling the extent of mutation in the whole global searching process. It provides a wide range of options for exploration and exploitation rates in the optimization process, such as a high exploration rate at the initial stage coupled with an increased exploitation rate at the later stage, or vice versa. Additionally, dynamic fluctuation of exploration and exploitation rates during the optimization process can also be achieved. Furthermore, it is worth mentioning that the PSO variant with no mutation is a special case for the AHMPSO, in which $p_{1c} = 0, p_{2c} = 0$ and $\mathbf{J}_{\bar{p}}$ is a vector with all elements of 1.

4. Stochastic Bandgap Optimization Framework on A Surrogate Model

To efficiently and effectively conduct the stochastic multiscale bandgap optimization for 3D EMMs involving microscale porosity and system uncertainties, which are two commonly observed manufacturing imperfections in an FDM part, a machine learning-aided framework is proposed. The newly developed framework consists of two main parts including *Part I: Surrogate model construction* and *Part II: Stochastic optimization for EMMs*, as shown in Figure 2.

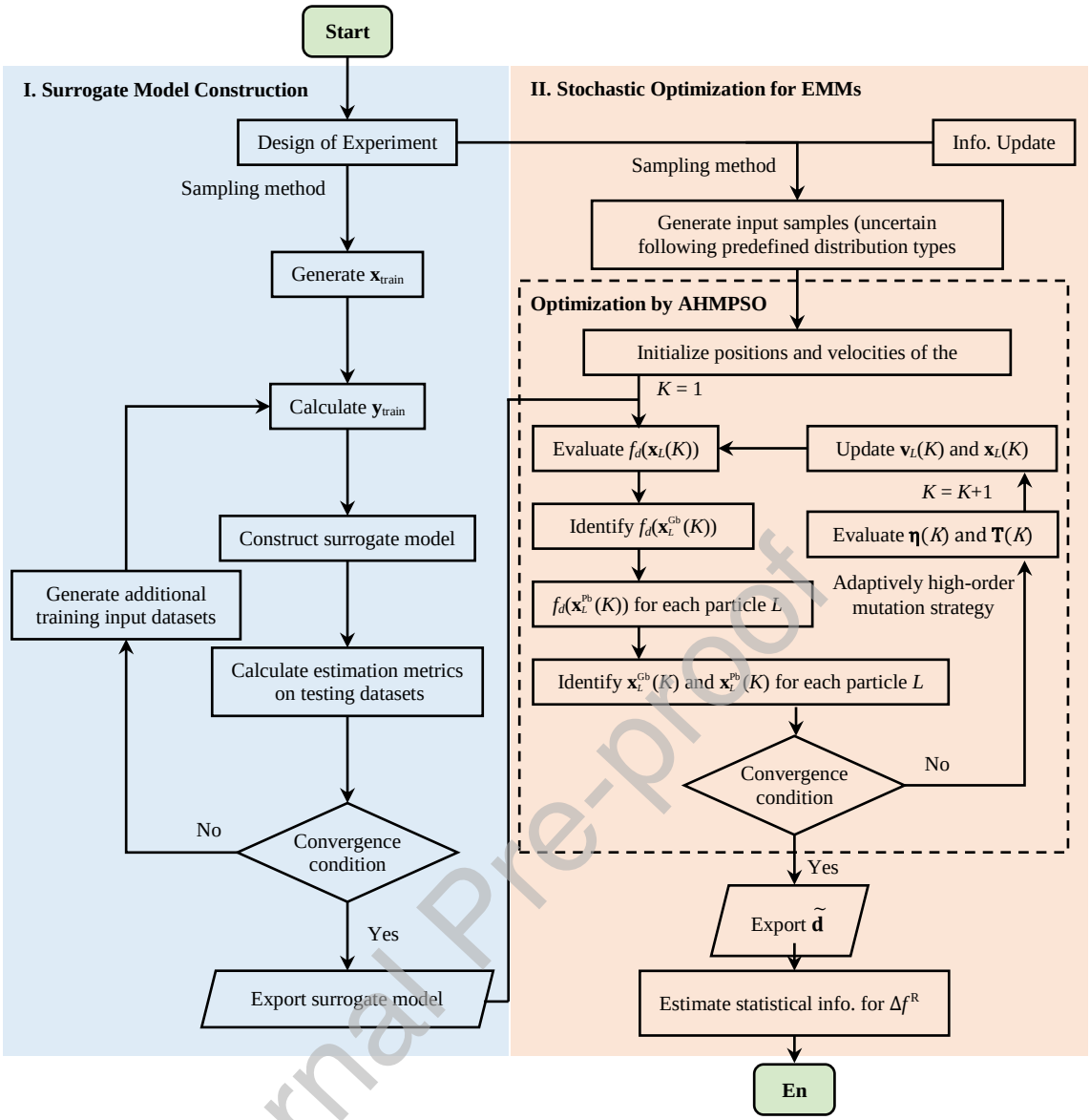

Figure 2: The proposed framework to implement the stochastic bandgap optimization by AHMPSO with the aid of surrogate models for EMMs with manufacturing imperfections.

In *Part I*, the main purpose is to establish an effective surrogate model, which bridges the underpinned relationship between multiscale structural parameters and concerned structural response, i.e., Δf . The surrogate model construction is started from the design of the experiment to clarify the physical problems, concerned structural response, boundaries of design variables, and statistical information of uncertainties. To generate training dataset input $\mathbf{x}_{\text{train}}$ that are specific realizations for $\boldsymbol{\xi}^{\text{R}}$ and $\mathbf{d}^{\text{R}}$, sampling methods, such as Latin hypercube sampling (LHC), Quasi-MCS, etc., can be employed [87]. The corresponding $\mathbf{y}_{\text{train}}$ is obtained by implementing numerical simulations through FE^2. Based on the developed training datasets, various machine-learning algorithms can be employed to establish surrogate models. In this paper, a recently published supervised machine learning algorithm, namely extended support vector regression (X-SVR) is adopted. Through solid mathematical support, surrogate model construction by the X-SVR algorithm is formulated into a quadratic programming

(QP) problem, which means that the global optimum can be obtained by any QP or convex solver [43]. In addition, to ensure the accuracy of the estimation, cross-validation is adopted to avoid overfitting. Furthermore, to tune the hyperparameters efficiently and effectively, Bayesian optimization is adopted, which can solve the optimization problem with fewer iterations compared with the traditional grid searching algorithm [88-90].

Subsequently, *Part II* is executed to conduct the stochastic bandwidth optimization for EMMs involving manufacturing imperfections. The newly developed PSO variant, i.e., AHMPSO is employed to solve the optimization problem. In the optimization process, the developed surrogate model $\hat{f}$ is employed to estimate the concerned structural responses and further used to estimate f_d for each particle L at the Kth iteration, denoted as $\hat{f}_d\left(\mathbf{x}_L\left(K\right)\right)$. In this case, a series of cumbersome tasks in the traditional FE^2 are avoided, including domain discretization, meshing, sophisticated constitutive relationship evaluation for models at both scales and integration of physical models across scales. Therefore, the computational resources required in each multiscale bandgap analysis are sharply reduced. Consequently, it significantly improves the applicability of the sampling-based method to approximate the statistical information for random structural outputs. In addition, the developed adaptive high-order mutation strategy is employed for balancing the exploration and exploitation rate in the optimization process. At the end of the optimization, optimal design parameters are obtained, which are collected in a vector $\tilde{\mathbf{d}}$. Then, sufficient statistical information, such as means, standard deviations, PDFs, and CDFs can be estimated for the concerned random structural response in the optimal EMM. Since the stochastic optimization framework concerns the mean and standard deviation of the random structural response simultaneously, the optimal design is expected to achieve the optimal goal, demonstrating large bandwidth and high robustness of optimum under the presence of manufacturing imperfections.

Besides the high computational efficiency, one inherent feature of the framework is information update. Once the surrogate model is developed, concerned structural response and statistical information for concerned structural responses can be updated in an efficient and effective manner without re-running computationally expensive FE^2. This feature offers significant merits in computational efficiency to update the optimal design for an EMM involving uncertainties following multiple distribution types. Moreover, the developed framework possesses high compatibility, which supports various machine learning methods and optimization algorithms. Furthermore, various data-processing techniques and post-processing techniques can be integrated into the framework [36].

5. Numerical Investigation

To demonstrate the computational stability, convergence speed and capability in global searching of the proposed AHMPSO, the computational performance of the algorithm is tested on benchmark problems in Section 5.1. In addition, to illustrate the efficiency, applicability and robustness of the developed framework, AHMPSO is implemented to solve the stochastic optimization for a 3D EMM involving manufacturing imperfections in Section 5.2.

5.1. AHMPSO on Benchmark Functions

The computational performance of the proposed AHMPSO is tested on two multi-dimensional multimodal benchmark problems, including Griewank and Rastrigin functions [91]. These benchmark functions have multiple local optimal, and the number

of local optimal increases exponentially as the increase of dimensionality, which is suitable for evaluating the performance of the optimization algorithm in global searching. The corresponding functions, search spaces, dimensionalities, and optimum values of the two benchmark functions are shown in Table 1.

Table 1: Benchmark functions.

Function	Expression	Dimensionality	Range	Optimum
Griewank	$f(x)=1+\sum_{i=1}^{D}\frac{x_i}{4000}-\prod_{i=1}^{D}\cos\left(\frac{x_i}{\sqrt{i}}\right)$	50	[-600,600]	0
Rastrigin	$f(x)=10D+\sum_{i=1}^{D}\left(x_i^2-10\cos(2\pi x_i)\right)$	50	[-50,50]	0

To compare the performance of the newly proposed AHMPSO with other PSO variants, LPSO-TVAC [84] and LHNPSO [85], are also implemented. The control parameters in the three algorithms for solving the benchmark problems are demonstrated in Table 2.

Table 2: The control parameters in three PSO variants.

Algorithm	Control parameters
LPSO-TVAC	$w_{\max}=0.9, w_{\min}=0.4, c_{1i}=c_{2f}=2.5, c_{1f}=c_{2i}=0.5$
LHNPSO	$w_{\max}=0.9, w_{\min}=0.4, c_{1i}=c_{2f}=2.5, c_{1f}=c_{2i}=0.5, \alpha=1/\pi^2, \beta=1, \gamma=1$
AHMPSO (Griewank)	$w_{\max}=0.9, w_{\min}=0.4, c_{1i}=c_{2f}=2.5, c_{1f}=c_{2i}=0.5, \alpha=1/\pi^2, \beta=1, \gamma=1$ $p_{1c}=1, \mathbf{J}_{50}=[1,1,\ldots,1]\in\Re^{50}, p_{c2}=1, \hbar=1, \phi=1$
AHMPSO (Rastrigin)	$w_{\max}=0.9, w_{\min}=0.4, c_{1i}=c_{2f}=2.5, c_{1f}=c_{2i}=0.5, \alpha=1/\pi^2 \beta=1, \gamma=1, p_{1c}=1,$ $\mathbf{J}_{50}=[0,0,\ldots,0]\in\Re^{50}, p_{c2}=1, \hbar=1, \phi=1$

Each benchmark problem is solved repeatedly for 20 times with an increased maximum iteration (i.e., 5, 10, 20, 40 and 60) to demonstrate the convergence speed and computational stability of the three algorithms. The population size is set as 20 in the three methods. In addition, the convergence plots are shown, illustrating the convergence trends of the best, mean, and worst optimal values when the maximum iteration is set as 20 and 10 for Griewank and Rastrigin functions, respectively. The computational results are summarized in Figures 3 and 4.

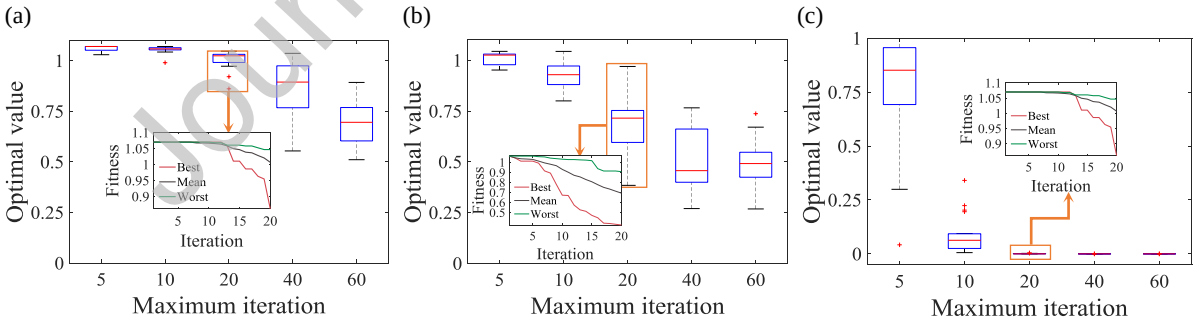

Figure 3: Optimal values for Griewank function solved by (a) LPSO-TVAC, (b) LHNPSO, (c) AHMPSO for 20 times when the population size is 20 and the maximum iterations are 5, 10, 20, 40 and 60, respectively.

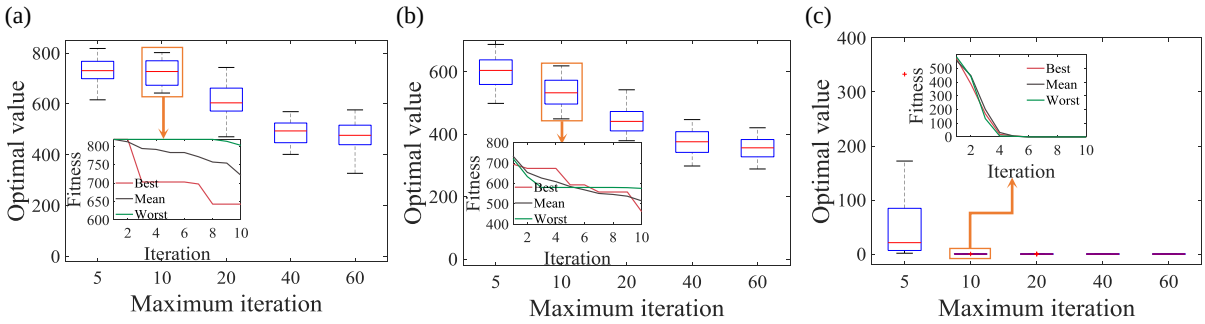

Figure 4: Optimal values for Rastrigin function solved by (a) LPSO-TVAC, (b) LHNPSO, (c) AHMPSO for 20 times when the population size is 20 and the maximum iterations are 5, 10, 20, 40, and 60, respectively.

It is illustrated from Figures 3 and 4 that the proposed AHMPSO has superior performance in convergence speed compared with LPSO-TVAC and LHNPSO. By only using 20 and 10 iterations to solve Griewank and Rastrigin functions, respectively, the proposed AHMPSO can find the nearly global optimum with exceptional computational stability, by referencing the extremely thin boxes around the global minimum at 0. Nonetheless, the solved optimal values by employing LPSO-TVAC and LHNPSO are significantly higher than the global minimum for both benchmark problems. Furthermore, the exceptional convergence speed of the proposed AHMPSO is demonstrated by the convergence plots. In summary, the introduced adaptively high-order mutation-based strategy significantly speeds up the convergence rate and enhances global searching ability with exceptional computational stability.

5.2. Stochastic Multiscale Optimization for a 3D Elastic Metamaterial (EMM)

To illustrate the applicability, computational efficiency and robustness of the proposed machine learning-aided framework on stochastic multiscale optimization for EMMs with manufacturing imperfections, a practically motivated case is implemented on a lattice-based 3D EMM involving both material and geometrical uncertainties. Before conducting the stochastic multiscale optimization on the 3D EMM, a deterministic multiscale bandgap analysis is performed to demonstrate the procedure by FEM, which is shown in Section 5.2.1. The results of the stochastic optimization are discussed in Section 5.2.2.

5.2.1. 3D Elastic Metamaterial (EMM) Design and its Deterministic Multiscale Bandgap Analysis

In order to reveal the bandgap characteristics of the FDM-manufactured 3D EMM, a multi-level numerical approach, consisting of two stages of homogenization, is employed to conduct the multiscale bandgap analysis for EMMs, as shown in Figure 5.

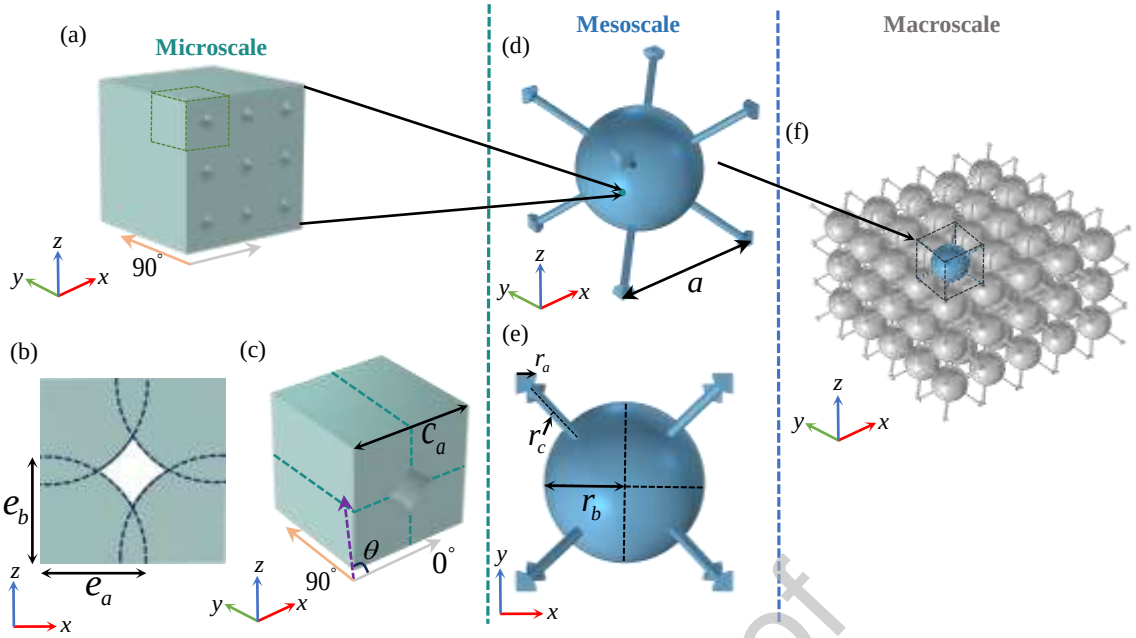

Figure 5: The multi-level approach for a 3D EMM with manufacturing imperfections. (a) An $3\times3\times3$ array of the microscale RVE; structural layout of the microscale RVE with θ of $90°$ in the (b) 2D view and (c) 3D view; structural layout of the mesoscale 3D EMM unit cell in the (d) 3D view and (e) 2D view; (f) 3D EMM array at the macroscale.

In the first stage of homogenization, to mimic the porosity distribution in the FDM-printed parts, a cubic RVE, shown in Figure 5(c), is developed to calculate the homogenized material properties for FDM-fabricated parts. The microscale RVE is characterized by seven structural parameters, including three material parameters, i.e., Young's modulus E, Poisson's ratio ν, density ρ, and four geometrical parameters including raster angle θ, RVE side length c_a, radii of the elliptical shape e_a and e_b from the cross-section of the deposited filaments. To derive the homogenized elasticity matrix, periodic boundary conditions are applied on the opposing faces in the RVE, and six loading cases are considered. To demonstrate the results, a numerical study is carried out on the RVE with structural parameters of 2GPa for E, 1150 kg/m^3 for ρ, 0.4 for υ, 0.06mm for C_a, 45° for θ, 0.035mm for both e_a and e_b, respectively. It is worth mentioning that the unit cell size of the microscale RVE needs to be significantly smaller than the EMM unit cell at the mesoscale to properly evaluate the material properties based on the homogenization method, indicating that only small-size porosity is considered in this work. The corresponding displacement filed in the RVE under six loading cases is shown in Figure 6(a-f).

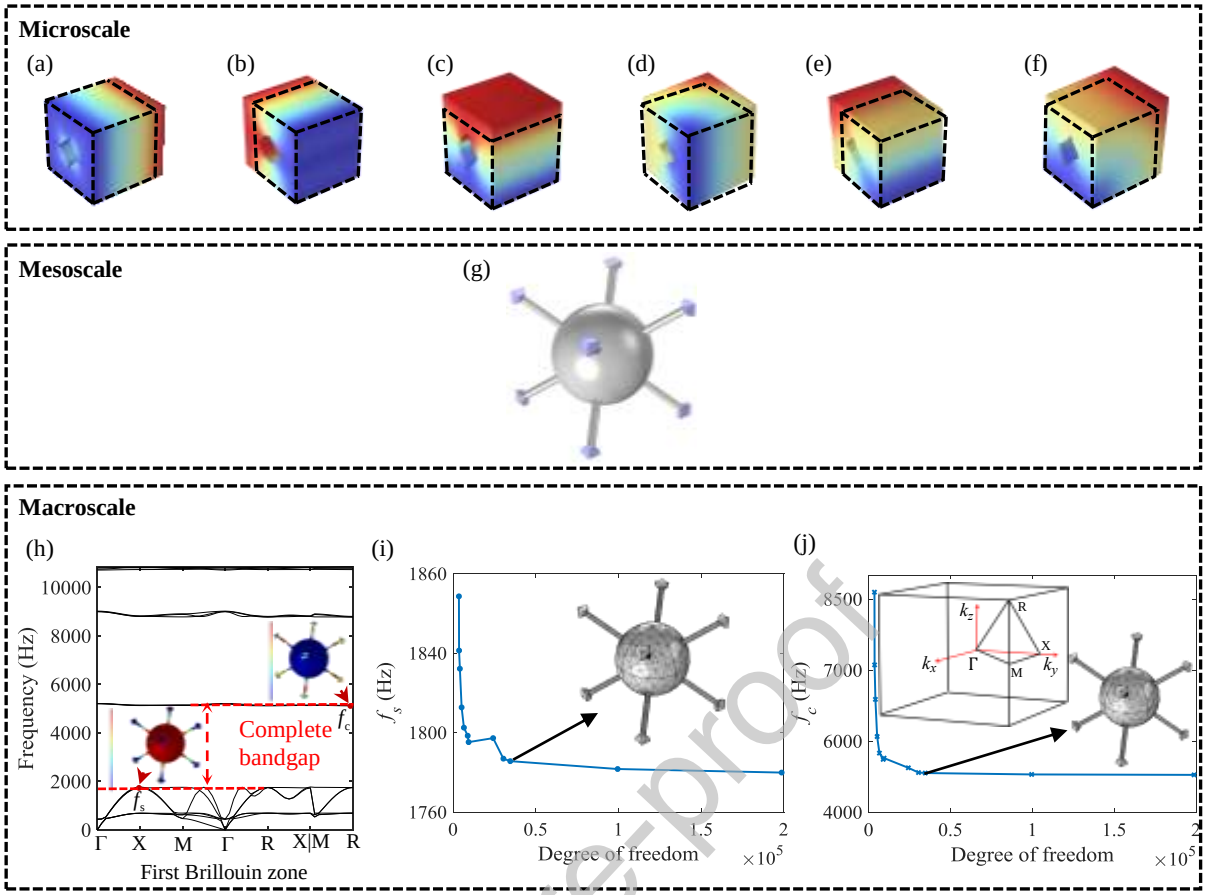

Figure 6: Displacement field of the microscale RVE under loading at (a) *x*-direction, (b) *y*-direction, (c) *z*-direction, (d) *xy*-direction, (e) *yz*-direction and (f) *xz*-direction; (g) mesoscale EMM unit cell with periodic boundary conditions coloured in blue; (h) band structure along for the 3D EMM at macroscale the k-path Γ-X-M-Γ-R-X|M-R of the macroscale 3D EMM; convergence study and the adopted mesh for (i) f_s, (j) f_c for the 3D EMM considering inter-bead porosity and structural parameters of a = 30mm, r_a = 3mm, r_b = 11mm, r_c = 0.8mm, $\hat{\rho}$ = 1073.41 kg/m^3.

The elasticity matrix derived based on the microscale RVE is calculated as:

$$\begin{bmatrix} 3.526e9 & 1.908e9 & 1.908e9 & 0 & 15404 & 0 \\ 1.908e9 & 3.005e9 & 1.766e9 & 0 & 14992 & 0 \\ 1.908e9 & 1.766e9 & 3.005e9 & 0 & 23518 & 0 \\ 0 & 0 & 0 & 6.537e8 & 0 & 911.890 \\ 15404 & 14992 & 23518 & 0 & 6.484e8 & 0 \\ 0 & 0 & 0 & 911.890 & 0 & 6.537e8 \end{bmatrix} \text{pa} \quad (42)$$

Subsequently, the derived elasticity matrix is applied to the mesoscale EMM unit cell, illustrated in Figure 6(g), which is characterized by four geometrical parameters, including unit cell size a, cornered sphere radius r_a, centered sphere radius r_b, and cylinder radius r_c. The second homogenization process is carried out by applying Floquet-Bloch periodic conditions on the opposing boundary surfaces of the mesoscale EMM unit cell, coloured in blue, to calculate the concerned bandgap properties for the macroscale 3D EMM [6]. In addition, due to the presence of porosity, the density of the

homogenized material, denoted as $\hat{\rho}$ is calculated as $\hat{\rho} = V_f \rho$ by the rule of mixture, and V_f denotes the volume fraction of the filament in the microscale RVE [21]. The deterministic bandgap solution for the EMM is obtained by sweeping the wavevector along the **k**-path Γ-X-M-Γ-R-X|M-R in the first Brillouin zone; Γ represents the centre of the Brillouin zone, M the centre of the edge, R a corner point, and X the centre of a face, respectively. Since the derivation of the **k**-path is the secondary problem in this research, the detailed derivation can be referred to the references [81,92,93]. The coordinates for $\Gamma, \mathrm{M}, \mathrm{R}$ and X are (0, 0, 0), $(\pi/a, \pi/a, 0)$, $(\pi/a, \pi/a, \pi/a)$ and (0, π/a, 0), respectively. The convergence study of the mesh is shown in Figure 6(i) and 6(j) for f_s and f_c, respectively, for an EMM with a = 30mm, r_a = 3mm, r_b = 11mm, r_c = 0.8mm, $\hat{\rho}$ = 1073.41 kg/m^3. According to Figures 6(i) and 6(j), it can be found that obvious convergence trends for both f_s and f_c are observed when the degree of freedom reaches 34497. In addition, from Figure 6(h), the 1st complete bandgap is identified as the lowest frequency range with no eigenfrequency, characterized by two quantities including the f_s and f_c with values of 1769.66 and 5145.94 Hz respectively. The NB is calculated as 97.94%. The operating wavelength for the first complete bandgap, which is capable of attenuating both longitudinal and transverse waves, is approximately 25 times larger than the size of the EMM unit cell, corresponding to the low-frequency bandgap.

5.2.2. Stochastic Multiscale Bandgap Optimization for a 3D Elastic Metamaterial (EMM)

Stimulated by practical implications, material and geometrical uncertainties are inherent features in 3D printed engineering structures, which greatly influence their mechanical and dynamic properties. Herein, to explore the optimum 3D EMMs involving manufacturing imperfections, a stochastic optimization is conducted on a multiscale 3D EMM involving material and geometrical uncertainties. Specifically, in this section, an effective surrogate model to bridge the relationship between structural parameters and NB is developed. Then, the stochastic optimization results for 3D EMMs involving manufacturing imperfections by the developed AHMPSO are discussed.

To establish an effective surrogate model, revealing the relationship between multiscale structural parameters and the concerned structural response, training datasets are generated by numerical methods. The training input dataset is generated through LHS for mutually independent variables within the ranges of [1.90e9, 2.10e9] Pa for E, $[1093.25, 1207.50]$ kg/m^3 for ρ, [0.38, 0.42] for υ, $\left[0^\circ, 90^\circ\right]$ for θ, [2.85, 3.15]mm for r_a, [11.40, 12.60]mm for r_b, [0.76, 0.84]mm for r_c, [0.033, 0.036] for both e_a and e_b, respectively. The corresponding training dataset outputs are obtained through performing the multiscale bandgap analysis by using COMSOL and the re-meshing in each realization is by the auto-mesh. A convergence study is conducted to explore the training sample size for the effective surrogate model. The computational accuracy of the model is assessed based on the estimation metrics listed in Table 3.

Table 3: Estimation metrics.

Estimation metric	Formulation

R-squared (R^2)	$R^2 = 1 - \frac{\sum_N \left(Y - \hat{Y}\right)^2}{\sum_N \left(Y - \bar{Y}\right)^2}$
Root Mean Square Error ($RMSE$)	$RMSE = \sqrt{\frac{\sum_N \left(Y - \hat{Y}\right)^2}{N}}$
Relative Error (RE)	$RE = \frac{Y - \hat{Y}}{Y} \times 100\%$

* where $Y, \hat{Y}$ and $\bar{Y}$ denote the FEM-based MCS results, surrogate model estimation, and the mean of the FEM-based MCS results respectively; N represents the number of samples.

In the convergence study, surrogate models with adjusted training sample sizes (i.e., 5, 25, 50, 100, 150, 200) are established. To demonstrate the computational stability, a mutually independent calculation is repeated 20 times. Furthermore, the best, mean, and worst values of R^2 and RMSE obtained in 20 runs are plotted versus different sample sizes. Besides the X-SVR method, other popular machine learning techniques, such as support vector regression (SVR) and neural network (NN) are implemented for comparisons, in terms of convergence speed and computational accuracy. To assess the accuracy, the brute MCS with 1e3 iterations is conducted as the reference. The computational results are summarized in Figure 7.

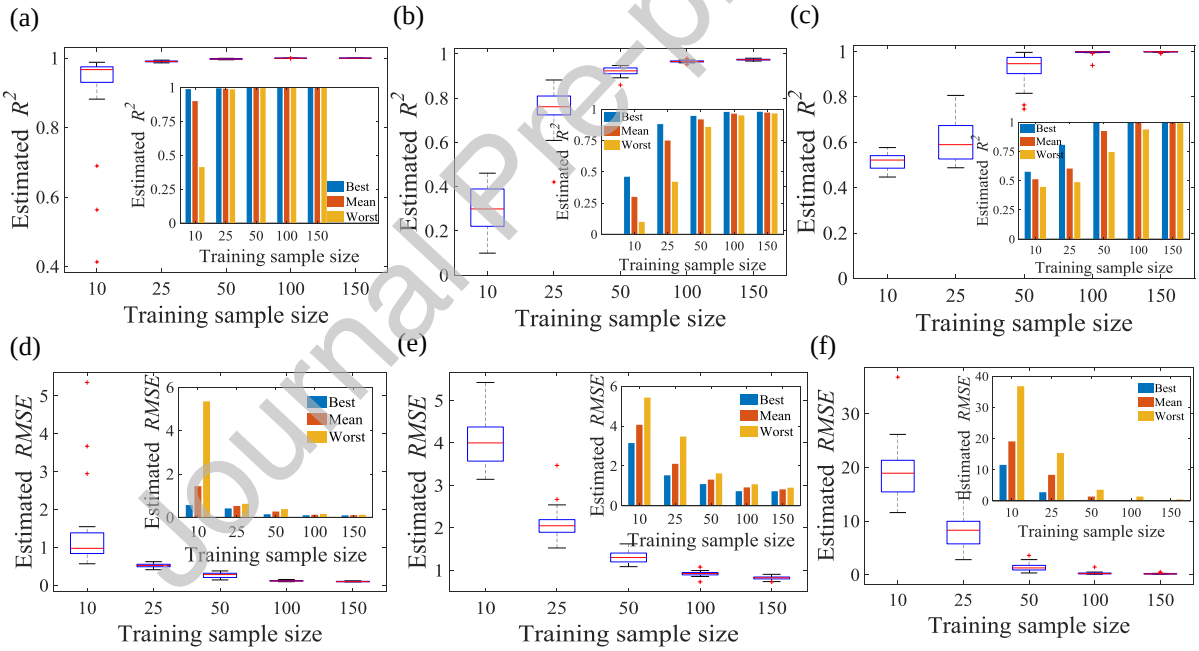

Figure 7: Convergence study, best, mean, and, worst values of estimated R^2 for surrogate models by (a) X-SVR, (b) SVR and (c) NN; estimated *RMSE* for surrogate models by (d) X-SVR, (e) SVR and (f) NN of NB for 3D EMMs considering inter-bead porosity and system uncertainties following uniform distributions when the training sample size is 10, 25, 50, 100, and 150.

According to the convergence study in Figure 7, it is noted that obvious convergence trends for R^2 and *RMSE* are observed for the models developed by the three machine learning algorithms. Effective surrogate models are established when the training sample size reaches 100. In the box plots, the thickness of the box represents the dispersion of the results and the '+' indicates the outlier. It is noted that the X-SVR

method possesses the highest computational stability compared with SVR and NN, by referencing to the thinnest boxes and least outliers. Furthermore, when the training sample size is 100, among the three developed models, the X-SVR method illustrates superior performance in computational accuracy by referring to the higher R^2 with a value of 0.9971 and lower *RMSE* at 0.2826 compared with the models by SVR and NN. Once the effective surrogate model is developed, a series of cumbersome and time-consuming tasks in the multi-level numerical approach are no longer involved, including domain discretization, meshing, evaluating the sophisticated constitutive relationships in two homogenization processes and the integration of FEM models across the scales. The estimation of structural response in the following analysis can be executed with significantly lowered computational expenses yet little sacrifice in accuracy. Therefore, in the following calculations, the developed surrogate model trained by 100 training samples is adopted to estimate NB for 3D EMMs with manufacturing imperfections.

Subsequently, to further demonstrate the high computational accuracy, the statistical information at 7 concerned locations, i.e., $\mu, \mu \pm \sigma, \mu \pm 2\sigma$ and $\mu \pm 3\sigma$ are estimated by the developed surrogate models. The brute MCS with 4e3 iterations are presented for reference.

Table 4: The estimated statistical information of NB for 3D EMMs involving inter-bead porosity and system uncertainties following uniform distributions. (Unit: %)

Location	**MCS**	**X-SVR**	***RE***	**SVR**	***RE***	**NN**	***RE***
$\mu-3\sigma$	80.0668	80.0476	-0.0240	81.8153	2.184	81.3854	1.65
$\mu-2\sigma$	85.4489	85.4392	-0.0113	86.6698	1.429	86.3445	1.05
$\mu-\sigma$	90.8310	90.8309	-1.480e-4	91.5244	0.763	91.3036	0.520
μ	96.2131	96.2225	0.00980	96.3789	0.172	96.2627	0.0515
$\mu+\sigma$	101.5952	101.6142	0.0187	101.2334	-0.356	101.2217	-0.368
$\mu+2\sigma$	106.9773	107.0058	0.0267	106.0880	-0.831	106.1808	-0.745
$\mu+3\sigma$	112.3594	112.3975	0.0339	110.9425	-1.26	111.1399	-1.085

From Table 4, it can be seen that the concerned statistical information is estimated accurately by the surrogate model through the X-SVR method. The maximum absolute value of *RE* is only 0.0339%, which is significantly lower than the values of 2.184% and 1.65% of SVR and NN, respectively. Hence, it is concluded that the X-SVR method possesses exceptional computational accuracy in estimating the structural performance and statistical information for 3D EMMs with manufacturing imperfections.

Then, PDFs and CDFs are generated to further highlight the computational accuracy of the three developed surrogate model. The exhaustive MCS with 4e3 iterations is employed as the benchmark for assessing the accuracy. In addition, the scatter plots are generated to demonstrate the dispersion of the results by surrogate models in reference to MCS results. The corresponding results are shown in Figure 8.

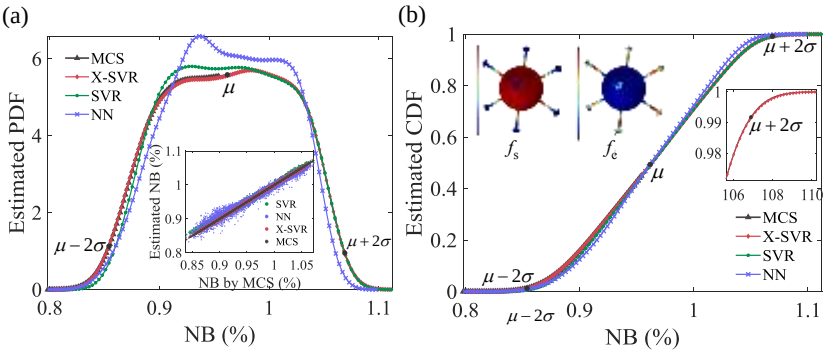

Figure 8: Estimated (a) PDF, scatter plot and (b) CDF of NB for multiscale EMMs by MCS, X-SVR, SVR and NN involving inter-bead porosity and system uncertainties following uniform distributions; mode shapes at f_s and f_c for the 3D EMM with NB $\mu\pm3\sigma$.

From Figure 8, it is seen that the estimated PDF and CDF by X-SVR highly overlap with the MCS results, demonstrating its exceptional computational accuracy in estimating NB for a multiscale EMM. Moreover, the high computational accuracy is shown by the highly overlapped results between X-SVR and MCS in the scatter plot. Besides, one inherent feature of the X-SVR method with high robustness is the information update. Without rerunning the computationally expensive numerical simulations, the trained X-SVR model can be used to estimate structural responses for 3D EMMs with inter-bead porosity and system uncertainties following multiple distribution types. To demonstrate it, the structural parameters in the EMM are modelled as random variables following various distribution types. The corresponding statistical information of the system uncertainties is shown in Table 5.

Table 5: Statistical information of material and geometrical uncertainties.

Parameter	Distribution type	Mean	Standard deviation	Range
E (GPa)	Normal	2.00	1.97e-2	[1.91, 2.07]
$\rho(\mathrm{g/cm^3})$	Gamma	1.15	1.16e-2	[1.10, 1.19]
υ	Extreme value	0.40	2.07e-2	[0.38, 0.40]
e_a (mm)	Logistic	0.035	2.471e-4	[0.034, 0.036]
e_b (mm)	Gamma	0.035	3.55e-3	[0.034, 0.036]
θ (°)	Lognormal	45	4.49	[30, 69]
r_a (mm)	Logistic	3.00	2.11e-2	[2.88, 3.13]
r_b (mm)	Lognormal	11.00	0.11	[10.59 ,11.40]
r_c (mm)	Extreme value	0.80	3.43e-3	[0.78, 0.81]

To quantify the performance in computational accuracy of the surrogate models developed through three machine learning methods, R^2 and *RMSE* are estimated in reference to the exhaustive MCS with 5e3 iterations. Moreover, the 7 concerned statistical information, i.e., $\mu, \mu\pm\sigma, \mu\pm2\sigma$ and $\mu\pm3\sigma$ of NB, are estimated. The corresponding computational results are summarized in Table 6.

Table 6: Estimation metrics for the developed surrogate models and estimated statistical information of NB by MCS, X-SVR, SVR and NN. (Unit: %)

	MCS	**X-SVR**	***RE***	**SVR**	***RE***	**NN**	***RE***
$\mu-3\sigma$	90.3923	90.5350	0.1579	91.3871	1.1006	90.9475	0.6142

$\mu-2\sigma$	92.2098	92.3395	0.1407	93.0243	0.8832	92.6575	0.4855
$\mu-\sigma$	94.0274	94.1440	0.1241	94.6614	0.6743	94.3675	0.3617
μ	95.8449	95.9486	0.1081	96.2986	0.4733	96.0775	0.2427
$\mu+\sigma$	97.6625	97.7531	0.0928	97.9357	0.2798	97.7875	0.1280
$\mu+2\sigma$	99.4800	99.5576	0.0780	99.5729	0.0934	99.4976	0.0179
$\mu+3\sigma$	101.2976	101.3621	0.0637	101.2101	-0.0864	101.2076	-0.0889
R^2	N/A	0.99576	N/A	0.94256	N/A	0.95857	N/A
RMSE	N/A	0.11745	N/A	0.44649	N/A	0.35796	N/A

It is noticed in Table 6 that the X-SVR technique possesses significantly higher R^2 and lower *RMSE* compared with the values from SVR and NN. In addition, the estimated absolute maximum *RE* for the statistical information by X-SVR is greatly lower than the corresponding values by SVR and NN, implying the exceptional performance in computational accuracy and robustness of the X-SVR method.

Besides the high accuracy and robustness of the X-SVR method, it is worth mentioning the high computational efficiency of the machine learning method compared with the FEM-based multiscale analysis. All computations were carried out on a workstation with Intel(R) Core(TM) Gold 5215 CPU @ 2.54GH 2.49GHz. It consumed 147 hours to conduct the multiscale analysis with 1e3 iterations by FEM and 736 hours to update the concerned structural responses when system uncertainties follow various distribution types. Nonetheless, by using the X-SVR method, the majority of time was consumed by the dataset establishment, which took approximately 15 hours to establish the training dataset. Once the training datasets were developed, it took less than 30 seconds to complete the following tasks, including hyperparameter tuning, surrogate model construction, estimating structural response with 2e3 iterations, and updating structural response with 5e3 iterations. Generally, the computational costs were sharply reduced in comparison to the brute MCS method on FEM models. Since the stochastic optimization process involves abundantly performing multiscale bandgap analysis for approximating statistical moments, the embedded X-SVR technique significantly improves the applicability of the proposed framework for stochastic optimization on practical 3D EMMs.

The high robustness, computational accuracy, and efficiency of the X-SVR method are demonstrated. Subsequently, the proposed AHMPSO is incorporated with the developed surrogate model to conduct the stochastic optimization for the multiscale 3D EMM. The statistical information of the random variables, including E, ρ,υ,e_a and e_b are listed in Table 5. The lower and upper boundaries for the design variables are $[0°, 90°]$ for θ, [2.85, 3.15]mm for r_a, [10.45, 11.55]mm for r_b and [0.76, 0.84]mm for r_c. To estimate the statistical information for the random NB, the MCS with 1e6 iterations is conducted on the surrogate models. The settings in the AHMPSO to solve the stochastic optimization problem are the same for the settings solving for the Griewank test function shown in Table 2, in which $\hbar$ and ϕ are changed to $1/\pi^2$ and 2, respectively. The number of particles and maximum iterations are both set as 40. To test the computational stability and convergence speed, the stochastic optimization problem is solved 20 times when w_s is set as 0.7. The convergence plots for the best, mean and worst fitness values found by AHMPSO are illustrated in Figure 9(a). In addition, the

estimated PDF and CDF for NB at the 1st and 40th iterations are shown in Figures 9(b) and 9(c), respectively. The mean and standard deviation for the concerned structural response at the 1st and 40th iterations are denoted as μ_1, σ_1 and μ_{40} and σ_{40} respectively.

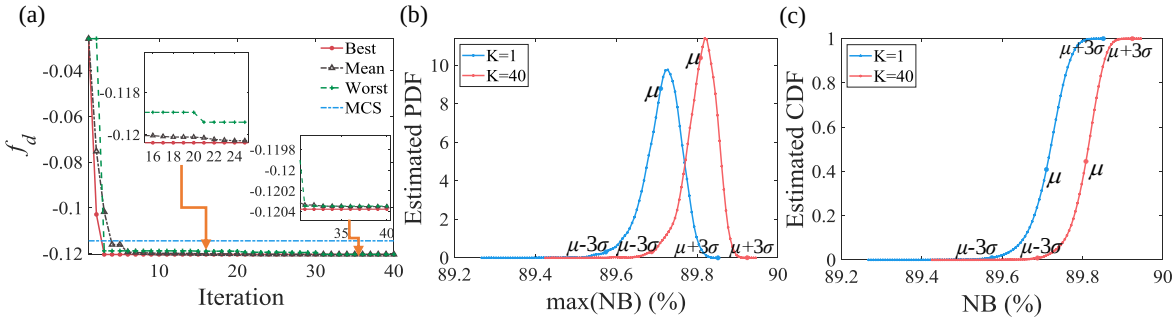

Figure 9: (a) The estimated optimal value by MCS with 1e6 iterations and convergence of the best, mean and worst fitness of the multiscale optimization for 3D EMMs involving inter-bead porosity and system uncertainties following multiple distribution types by the proposed AHMPSO for 20 times when w_s is 0.7 and both the maximum iteration and population size are set as 40; estimated (b) PDF and (c) CDF of the NB for a 3D EMM with inter-bead porosity and system uncertainties following multiple distribution types at the 1st and 40th iterations by the AHMPSO.

From Figure 9(a), an obvious convergence trend is noted when the maximum iterations reach 40 in all 20 runs. In addition, it is found that the optimal value solved by the AHMPSO outperforms the optimal value obtained from the brute MCS with 1e6 iterations, implying the extraordinary performance in global searching of AHMPSO for the stochastic optimization of the 3D EMM with manufacturing imperfections. Furthermore, in Figures 9(b) and 9(c), $\mu(\triangle f)$ is increased and $\sigma(\triangle f)$ is decreased simultaneously at the 40th iteration compared with the initial design, which indicates that the optimized EMM possesses higher applicability and robustness through the enlarged bandwidths and reduced variations in structural performance.

Subsequently, structural optimizations are undertaken for w_s varied from 0 to 1. The Pareto optimal regarding $\mu(\triangle f)$ and $\sigma(\triangle f)$ for EMMs is summarized in Figure 10(a). In addition, the estimated PDF and CDF by X-SVR at the the minimum standard deviation (w_s=1) and largest mean (w_s=0)are shown in Figure 10(b) and 10(c), respectively.

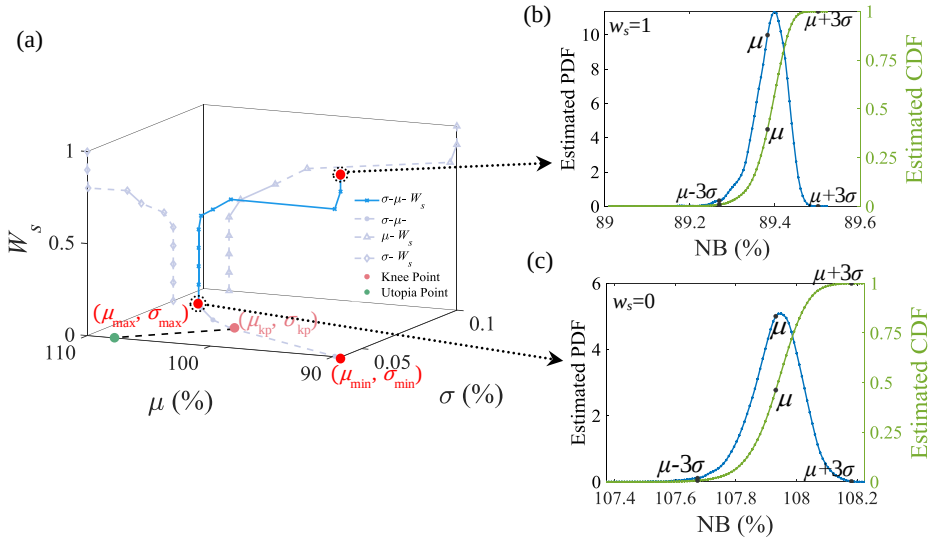

Figure 10: (a) Pareto optimal solutions for w_s varied from 0 to 1 and the knee point solved by AHMPSO for 3D EMMs considering inter-bead porosity and system uncertainties following multiple distribution types; estimated PDF and CDF for 3D EMMs when w_s is (b) 1 and (c) 0.

From Figure 10(a), it is found that the increase of μ leads to the increase of σ, implying the conflict between the two sub-objectives. The highest mean, i.e., μ_{max} is achieved when w_s is 0, which leads to a significant increase of σ, implying large variations of structural performance. Similarly, when the minimum standard deviation, i.e., σ_{min} is achieved, μ is decreased extensively by more than 17%, which detrimentally affects the applicability of EMMs for real-life applications. Even the Pareto-set solutions in Figure 10(a) offer a large number of design solutions, a decision must be made for the most satisfactory solution. Hence, a knee point is found, which has the minimum distance to the utopia point, i.e., optimal values of each individual objective. The identified knee point is marked in Figure 10(a), which has corresponding w_s of 0.72. The corresponding estimated μ and σ for the NB are 101.2542% and 0.0593%, respectively for the 3D EMM with manufacturing imperfections. The optimal design parameters for θ, r_a, r_b and r_c are 0°, 2.85mm, 11.11mm and 0.84mm respectively. The corresponding estimated PDF and CDF for the concerned structural response are shown in Figures 11(a) and 11(b). In addition, hypothesis testing for three common probability distributions, including Extreme value, Loglogistic, and Lognormal are implemented.

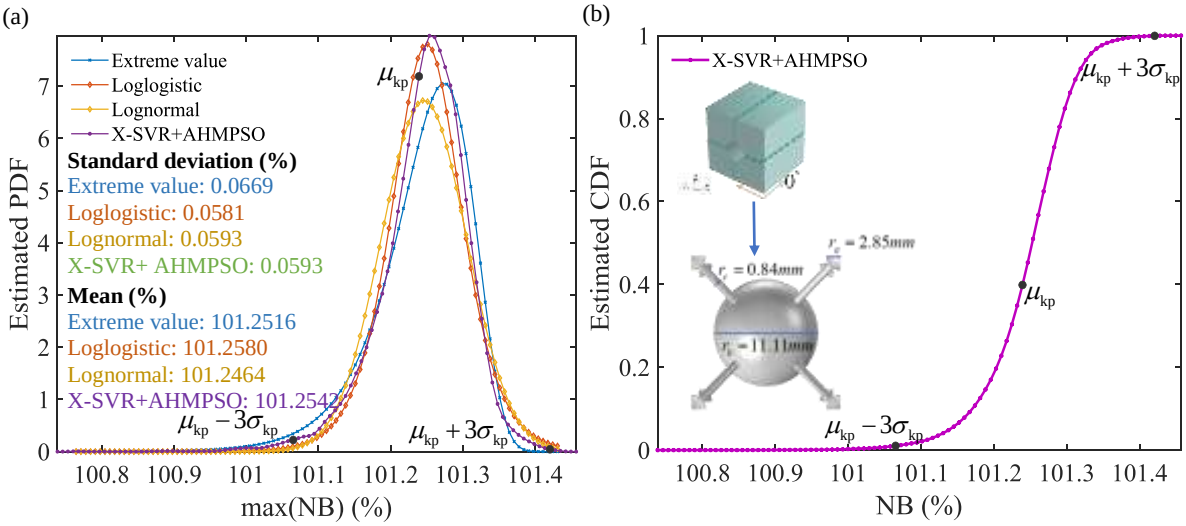

Figure 11: (a) Hypothesis test and the estimated PDF by the proposed framework with embedded X-SVR and AHMPSO and (b) CDF of NB at the knee point for a 3D EMM considering inter-bead porosity and system uncertainties following multiple distribution types.

From Figure 11(a), it can be found that although the means and standard deviations from the four distributions are extremely close, especially from the Lognormal distribution, the fitted PDF by the hypothesized probability distribution cannot accord with the results from the MCS-based approach (X-SVR incorporated with AHMPSO). As for the relationship between multiscale system variables and the concerned structural responses for the optimized multiscale 3D EMM is highly nonlinear, it is extremely challenging to pre-assume the distribution type of the concerned structural response. With the aid of the proposed framework, i.e., machine learning-aided approach, there is no prerequisite on the distribution type of the concerned output. By importing the statistical information of random variables into the framework, the multiscale EMMs with manufacturing imperfections can be optimized, demonstrating large bandwidths with small variations in structural responses, which exhibit high applicability and robustness of the optimum. Furthermore, sufficient information, including statistical moments, PDF, and CDF of the concerned structural response for the EMM can be estimated.

6. Conclusions

In this paper, a novel sampling-based stochastic multiscale optimization framework is developed for EMMs considering manufacturing imperfections, including microscale porosity and system uncertainties simultaneously. Instead of optimizing a single value of the normalized bandwidth (NB), the first two statistical moments are optimized, aiming at improving applicability and robustness to the optimum of 3D EMMs simultaneously. Within the framework, a machine learning method, i.e., namely the extended support vector regression (X-SVR) is embedded to relieve the large computational cost of estimating the first two statical moments for 3D EMMs with manufacturing imperfections. Subsequently, a new particle swarm optimization (PSO) variant, i.e., adaptively high-order mutation-based particle swarm optimization (AHMPSO) is introduced to solve the stochastic optimization problem. The computational accuracy, robustness, and applicability of the framework are demonstrated by numerical investigations.

Effective surrogate models by the X-SVR method, bridging the structural parameters and the NB for 3D EMMs, successfully substitute a series of complicated tasks involved in the FE^2 for multiscale bandgap analysis. Furthermore, in the numerical investigation, the X-SVR method is superior to SVR and NN in terms of convergency speed, computational stability, and computational accuracy. Furthermore, the adopted X-SVR method possesses high robustness, which is capable of accurately estimating the bandwidths for the 3D EMMs when the distribution types of the system uncertainties are changed, without rerunning the computationally costly physical models. The computational cost to estimate the statistical moments is significantly reduced compared with the traditional MCS method.

The introduction of the high-order functions in the PSO is demonstrated to effectively improve the convergency speed, global searching performance, and computational stability on both multimodal benchmark functions and the stochastic optimization problem for the 3D EMM, compared with LPSO-TVAC and LHNPSO. With the aid of the X-SVR and AMHPSO, Pareto optimal regarding the mean and standard deviation of the NB is obtained. Furthermore, sufficient statistical information, including the first two statistical moments, probability density function (PDF), and cumulative distribution function (CDF) of the NB for 3D EMMs with manufacturing imperfections are estimated effectively and efficiently.

In conclusion, under stochastic optimization, the multiscale 3D EMMs with manufacturing imperfections demonstrate large bandwidths coupling with high robustness of optimum. Persuasively, the advanced framework significantly benefits the analysis, optimization, and fabrication of EMMs in multi-disciplinary engineering applications.

Acknowledgement

The work presented in this paper has been supported by Australian Research Council projects IH210100048, IH200100010, DP210101353, and DP240102559.

Appendix A

In LPSO-TVAC, w, c_1 and c_2 are updated based on the formulations:

$$w(K+1) = w_{\max} - (w_{\max} - w_{\min})\left(\frac{K}{K_{\max}}\right) \qquad \text{(A.1)}$$

$$c_1(K+1) = c_{1i} - (c_{1i} - c_{1f})\left(\frac{K}{K_{\max}}\right) \qquad \text{(A.2)}$$

$$c_2(K+1) = c_{2i} - (c_{2i} - c_{2f})\left(\frac{K}{K_{\max}}\right) \qquad \text{(A.3)}$$

where c_{1i}, c_{if}, c_{2i} and c_{2f} are initial and final values of the cognitive and social parameters, respectively.

Appendix B

In LHNPSO, w, c_1 and c_2 are updated based on the formulations:

$$w(K+1) = w_{\max} - (w_{\max} - w_{\min})\left(\frac{K}{K_{\max}}\right)^{\alpha} \qquad \text{(B.1)}$$

$$c_1(K+1) = c_{1i} - (c_{1i} - c_{1f})\left(\frac{K}{K_{\max}}\right)^{\beta} \qquad \text{(B.2)}$$

$$c_2(K+1) = c_{2i} - (c_{2i} - c_{2f})\left(\frac{K}{K_{\max}}\right)^{\gamma} \qquad \text{(B.3)}$$

where α, β and γ are three parameters to control the variations of inertia weight and acceleration coefficients.

Reference

1. Wu, Z., et al., *Band-gap property of a novel elastic metamaterial beam with X-shaped local resonators.* Mechanical Systems Signal Processing, 2019. **134**: p. 106357.
2. Fan, X., et al., *Multi-bandgaps metamaterial plate design using complex mass-beam resonator.* International Journal of Mechanical Sciences, 2022. **236**: p. 107742.
3. Gorshkov, V.N., et al., *Acoustic metamaterials with controllable bandgap gates based on magnetorheological elastomers.* International Journal of Mechanical Sciences, 2023. **238**: p. 107829.
4. Li, Z., et al., *Three-dimensional metamaterials exhibiting extreme isotropy and negative Poisson's ratio.* International Journal of Mechanical Sciences, 2023: p. 108617.
5. Nobrega, E., et al., *Vibration band gaps for elastic metamaterial rods using wave finite element method.* Mechanical Systems Signal Processing, 2016. **79**: p. 192-202.
6. Zhang, M., et al., *Design of elastic metamaterials with ultra-wide low-frequency stopbands via quantitative local resonance analysis.* Thin-Walled Structures, 2021. **165**: p. 107969.
7. Zeng, Y., et al., *Seismic metamaterials: Generating low-frequency bandgaps induced by inertial amplification.* International Journal of Mechanical Sciences, 2022. **221**: p. 107224.
8. Kalderon, M., et al., *Locally resonant metamaterials utilizing dynamic directional amplification: An application for seismic mitigation.* Applied Mathematical Modelling, 2022. **110**: p. 1-16.
9. Wang, G., et al., *Enhancement of the vibration attenuation characteristics in local resonance metamaterial beams: Theory and experiment.* Mechanical Systems and Signal Processing, 2023. **188**: p. 110036.
10. Sugino, C., et al., *On the mechanism of bandgap formation in locally resonant finite elastic metamaterials.* Journal of Applied Physics, 2016. **120**(13).
11. Zhang, M., Y. Xiao, and Q.-H. Qin, *Modal-based analysis for aiding 3d elastic metastructure design.* International Journal of Applied Mechanics, 2023.
12. Zhu, R., et al., *A chiral elastic metamaterial beam for broadband vibration suppression.* Journal of Sound Vibration, 2014. **333**(10): p. 2759-2773.
13. Hao, S., et al., *A novel locally resonant metastructure with soft-material rings for broadband and low frequency vibration attenuation.* Engineering Structures, 2022. **272**: p. 114978.
14. Dong, J., et al., *Analysis of wave band gaps in mechanical metamaterial based on Nelder–Mead method.* Engineering Analysis with Boundary Elements, 2019. **103**: p. 109-115.
15. Yuksel, O. and C. Yilmaz, *Realization of an ultrawide stop band in a 2-D elastic metamaterial with topologically optimized inertial amplification mechanisms.* International Journal of Solids Structures, 2020. **203**: p. 138-150.

16. White, D.A., et al., *Multiscale topology optimization using neural network surrogate models.* Computer Methods in Applied Mechanics Engineering, 2019. **346**: p. 1118-1135.
17. Yan, G., et al., *Topological optimization of thin elastic metamaterial plates for ultrawide flexural vibration bandgaps.* International Journal of Mechanical Sciences, 2023. **242**: p. 108014.
18. Jiang, T., Q. Han, and C. Li, *Design and bandgap optimization of multi-scale composite origami-inspired metamaterials.* International Journal of Mechanical Sciences, 2023. **248**: p. 108233.
19. Yan, G., et al., *Multi-objective optimization of elastic metaplates for lightweight and ultrawide bandgaps.* International Journal of Mechanical Sciences, 2023: p. 108603.
20. Matlack, K.H., et al., *Composite 3D-printed metastructures for low-frequency and broadband vibration absorption.* Proceedings of the National Academy of Sciences, 2016. **113**(30): p. 8386-8390.
21. Dong, J., et al., *Structural optimisation of cross-chiral metamaterial structures via genetic algorithm.* Composite Structures, 2022. **282**: p. 115035.
22. Kennedy, J., et al., *The influence of additive manufacturing processes on the performance of a periodic acoustic metamaterial.* International Journal of Polymer Science, 2019. **2019**.
23. Isakov, D., et al., *3D printed anisotropic dielectric composite with meta-material features.* Materials & Design, 2016. **93**: p. 423-430.
24. Rajan, K., et al., *Fused deposition modeling: process, materials, parameters, properties, and applications.* The International Journal of Advanced Manufacturing Technology, 2022. **120**(3-4): p. 1531-1570.
25. Askari, M., et al., *Additive manufacturing of metamaterials: A review.* Additive Manufacturing, 2020. **36**: p. 101562.
26. Nimmagadda, C. and K.H. Matlack, *Thermally tunable band gaps in architected metamaterial structures.* Journal of Sound and Vibration, 2019. **439**: p. 29-42.
27. Hassen, A.A., et al., *Anisotropic thermal behavior of extrusion-based large scale additively manufactured carbon-fiber reinforced thermoplastic structures.* Polymer Composites, 2022. **43**(6): p. 3678-3690.
28. Penumakala, P.K., J. Santo, and A. Thomas, *A critical review on the fused deposition modeling of thermoplastic polymer composites.* Composites Part B: Engineering, 2020. **201**: p. 108336.
29. Charlon, S., J. Le Boterff, and J. Soulestin, *Fused filament fabrication of polypropylene: Influence of the bead temperature on adhesion and porosity.* Additive Manufacturing, 2021. **38**: p. 101838.
30. Iyer, S.S.G. and O. Keles, *Effect of raster angle on mechanical properties of 3D printed short carbon fiber reinforced acrylonitrile butadiene styrene.* Composites Communications, 2022. **32**: p. 101163.
31. Gauss, C. and K.L. Pickering, *A new method for producing polylactic acid biocomposites for 3D printing with improved tensile and thermo-mechanical performance using grafted nanofibrillated cellulose.* Additive Manufacturing, 2023. **61**: p. 103346.
32. Sola, A., et al., *Open challenges in tensile testing of additively manufactured polymers: a literature survey and a case study in fused filament fabrication.* Polymer Testing, 2023. **117**: p. 107859.

33. Dizon, J.R.C., et al., *Mechanical characterization of 3D-printed polymers.* Additive manufacturing, 2018. **20**: p. 44-67.
34. Awasthi, P. and S.S. Banerjee, *Fused deposition modeling of thermoplastic elastomeric materials: Challenges and opportunities.* Additive Manufacturing, 2021. **46**: p. 102177.
35. Boulvert, J., et al., *Acoustic modeling of micro-lattices obtained by additive manufacturing.* Applied Acoustics, 2020. **164**: p. 107244.
36. Wang, Q., et al., *Polymorphic uncertainty quantification for engineering structures via a hyperplane modelling technique.* Computer Methods in Applied Mechanics Engineering, 2022. **398**: p. 115250.
37. Heinecke, F. and C. Willberg, *Manufacturing-induced imperfections in composite parts manufactured via automated fiber placement.* Journal of Composites Science, 2019. **3**(2): p. 56.
38. Fina, M., P. Weber, and W. Wagner, *Polymorphic uncertainty modeling for the simulation of geometric imperfections in probabilistic design of cylindrical shells.* Structural Safety, 2020. **82**: p. 101894.
39. Berger, J., H. Wadley, and R. McMeeking, *Mechanical metamaterials at the theoretical limit of isotropic elastic stiffness.* Nature, 2017. **543**(7646): p. 533-537.
40. Beyer, H.-G. and B. Sendhoff, *Robust optimization–a comprehensive survey.* Computer methods in applied mechanics engineering, 2007. **196**(33-34): p. 3190-3218.
41. Doltsinis, I. and Z. Kang, *Robust design of structures using optimization methods.* Computer methods in applied mechanics engineering, 2004. **193**(23-26): p. 2221-2237.
42. Ben-Tal, A., L. El Ghaoui, and A. Nemirovski, *Robust optimization*. Vol. 28. 2009: Princeton university press.
43. Sánchez, D.M., et al., *Development of carbon fiber acrylonitrile styrene acrylate composite for large format additive manufacturing.* Materials Design, 2020. **191**: p. 108577.
44. Hu, C., et al., *The fabrication of long carbon fiber reinforced polylactic acid composites via fused deposition modelling: Experimental analysis and machine learning.* Journal of Composite Materials, 2021. **55**(11): p. 1459-1472.
45. Papon, E.A., A. Haque, and S.B. Mulani, *Process optimization and stochastic modeling of void contents and mechanical properties in additively manufactured composites.* Composites Part B: Engineering, 2019. **177**: p. 107325.
46. Sahinidis, N.V., *Optimization under uncertainty: state-of-the-art and opportunities.* Computers chemical engineering, 2004. **28**(6-7): p. 971-983.
47. Rahimian, H. and S. Mehrotra, *Frameworks and results in distributionally robust optimization.* Open Journal of Mathematical Optimization, 2022. **3**: p. 1-85.
48. Ribeiro, L., V. Dal Poggetto, and J. Arruda, *Robust optimization of attenuation bands of three-dimensional periodic frame structures.* Acta Mechanica, 2022. **233**(2): p. 455-475.
49. Jerez, D., H. Jensen, and M. Beer, *Reliability-based design optimization of structural systems under stochastic excitation: an overview.* Mechanical Systems and Signal Processing, 2022. **166**: p. 108397.
50. Sun, G., et al., *Multiobjective robust optimization method for drawbead design in sheet metal forming.* Materials design, 2010. **31**(4): p. 1917-1929.

51. Xian, J. and C. Su, *Stochastic optimization of uncertain viscous dampers for energy-dissipation structures under random seismic excitations.* Mechanical Systems and Signal Processing, 2022. **164**: p. 108208.
52. Dai, H., R. Zhang, and M. Beer, *A new method for stochastic analysis of structures under limited observations.* Mechanical Systems and Signal Processing, 2023. **185**: p. 109730.
53. Gao, W., et al., *Hybrid probabilistic interval analysis of bar structures with uncertainty using a mixed perturbation Monte-Carlo method.* Finite Elements in Analysis Design, 2011. **47**(7): p. 643-652.
54. Betz, W., I. Papaioannou, and D. Straub, *Bayesian post-processing of Monte Carlo simulation in reliability analysis.* Reliability Engineering & System Safety, 2022. **227**: p. 108731.
55. Choi, S.W., L.E. Gibbons, and P.K. Crane, *Lordif: An R package for detecting differential item functioning using iterative hybrid ordinal logistic regression/item response theory and Monte Carlo simulations.* Journal of statistical software, 2011. **39**(8): p. 1.
56. Zheng, Z., et al., *A stochastic finite element scheme for solving partial differential equations defined on random domains.* Computer Methods in Applied Mechanics Engineering, 2023. **405**: p. 115860.
57. Sun, T., et al., *Multiscale uncertainty propagation analysis and reliability optimization of the CFRP crossbeam of the twist beam axle.* International Journal of Mechanical Sciences, 2023. **242**: p. 108022.
58. Huang, L., H. Yuan, and H. Zhao, *An FEM-based homogenization method for orthogonal lattice metamaterials within micropolar elasticity.* International Journal of Mechanical Sciences, 2023. **238**: p. 107836.
59. Hasan, M.F., M.S. Zantye, and M.-K. Kazi, *Challenges and opportunities in carbon capture, utilization and storage: A process systems engineering perspective.* Computers & Chemical Engineering, 2022: p. 107925.
60. Afshari, S.S., et al., *Machine learning-based methods in structural reliability analysis: A review.* Reliability Engineering System Safety, 2022. **219**: p. 108223.
61. Sun, H., H.V. Burton, and H. Huang, *Machine learning applications for building structural design and performance assessment: State-of-the-art review.* Journal of Building Engineering, 2021. **33**: p. 101816.
62. Nguyen, L.C. and H. Nguyen-Xuan, *Deep learning for computational structural optimization.* ISA transactions, 2020. **103**: p. 177-191.
63. Jain, M., et al., *An overview of variants and advancements of PSO algorithm.* Applied Sciences, 2022. **12**(17): p. 8392.
64. Wang, Q., et al., *Machine learning aided stochastic structural free vibration analysis for functionally graded bar-type structures.* Thin-Walled Structures, 2019. **144**: p. 106315.
65. Wang, Q., et al., *Polyphase uncertainty analysis through virtual modelling technique.* Mechanical Systems Signal Processing, 2022. **162**: p. 108013.
66. Yu, Y., et al., *Machine learning aided durability and safety analyses on cementitious composites and structures.* International Journal of Mechanical Sciences, 2019. **160**: p. 165-181.
67. Plevris, V. and M. Papadrakakis, *A hybrid particle swarm—gradient algorithm for global structural optimization.* Computer-Aided Civil Infrastructure Engineering, 2011. **26**(1): p. 48-68.

68. Fister Jr, I., et al., *A Brief Review of Nature-Inspired Algorithms for Optimization.* ELEKTROTEHNIˇSKI VESTNIK, 2013. **80**(3): p. 116-122.
69. Ramírez-Ochoa, D.-D., et al., *PSO, a swarm intelligence-based evolutionary algorithm as a decision-making strategy: A review.* Symmetry, 2022. **14**(3): p. 455.
70. Sharma, A.K., et al., *Gradient-based topology optimization of soft dielectrics as tunable phononic crystals.* Composite Structures, 2022. **280**: p. 114846.
71. Sharma, I., V. Kumar, and S. Sharma, *A comprehensive survey on grey wolf optimization.* Recent Advances in Computer Science and Communications (Formerly: Recent Patents on Computer Science), 2022. **15**(3): p. 323-333.
72. Yang, X.-S., *Nature-inspired optimization algorithms*. 2020: Academic Press.
73. Abd-El-Wahed, W.F., A. Mousa, and M. El-Shorbagy, *Integrating particle swarm optimization with genetic algorithms for solving nonlinear optimization problems.* Journal of Computational Applied Mathematics, 2011. **235**(5): p. 1446-1453.
74. Stacey, A., M. Jancic, and I. Grundy. *Particle swarm optimization with mutation*. in *The 2003 Congress on Evolutionary Computation, 2003. CEC'03.* 2003. IEEE.
75. Higashi, N. and H. Iba. *Particle swarm optimization with Gaussian mutation*. in *Proceedings of the 2003 IEEE Swarm Intelligence Symposium. SIS'03 (Cat. No. 03EX706)*. 2003. IEEE.
76. Andrews, P.S. *An investigation into mutation operators for particle swarm optimization*. in *2006 IEEE International Conference on Evolutionary Computation*. 2006. IEEE.
77. Thangaraj, R., et al., *Particle swarm optimization: Hybridization perspectives and experimental illustrations.* Computational materials science, 2011. **217**(12): p. 5208-5226.
78. Nguyen, V.-D., et al., *Imposing periodic boundary condition on arbitrary meshes by polynomial interpolation.* Computational Materials Science, 2012. **55**: p. 390-406.
79. Jiang, H., et al., *Band gaps and vibration isolation of a three-dimensional metamaterial with a star structure.* Materials, 2020. **13**(17): p. 3812.
80. Collet, M., et al., *Floquet–Bloch decomposition for the computation of dispersion of two-dimensional periodic, damped mechanical systems.* International Journal of Solids Structures, 2011. **48**(20): p. 2837-2848.
81. Setyawan, W. and S. Curtarolo, *High-throughput electronic band structure calculations: Challenges and tools.* Computational materials science, 2010. **49**(2): p. 299-312.
82. Dunbar, M., et al., *Simultaneous classification and feature selection via convex quadratic programming with application to HIV-associated neurocognitive disorder assessment.* J European Journal of Operational Research, 2010. **206**(2): p. 470-478.
83. Kennedy, J. and R. Eberhart. *Particle swarm optimization*. in *Proceedings of ICNN'95-international conference on neural networks*. 1995. IEEE.
84. Ratnaweera, A., S.K. Halgamuge, and H.C. Watson, *Self-organizing hierarchical particle swarm optimizer with time-varying acceleration coefficients.* IEEE Transactions on evolutionary computation, 2004. **8**(3): p. 240-255.
85. Yang, C., et al., *Low-discrepancy sequence initialized particle swarm optimization algorithm with high-order nonlinear time-varying inertia weight.* Applied Soft Computing, 2015. **29**: p. 386-394.
86. Dong, W., L. Kang, and W. Zhang, *Opposition-based particle swarm optimization with adaptive mutation strategy.* Soft Computing, 2017. **21**: p. 5081-5090.

87. Blatman, G., B. Sudret, and M. Berveiller, *Quasi random numbers in stochastic finite element analysis.* Mechanics Industry, 2007. **8**(3): p. 289-297.
88. Snoek, J., H. Larochelle, and R.P. Adams, *Practical bayesian optimization of machine learning algorithms.* Advances in neural information processing systems, 2012. **25**.
89. Hawkins, D.M., *The problem of overfitting.* Journal of chemical information computer sciences, 2004. **44**(1): p. 1-12.
90. Wang, Q., et al., *Machine learning aided static structural reliability analysis for functionally graded frame structures.* Applied Mathematical Modelling, 2020. **78**: p. 792-815.
91. Zaman, H.R.R. and F.S. Gharehchopogh, *An improved particle swarm optimization with backtracking search optimization algorithm for solving continuous optimization problems.* Engineering with Computers, 2022. **38**(Suppl 4): p. 2797-2831.
92. Andrew, R.C., T. Salagaram, and N. Chetty, *Visualising higher order Brillouin zones with applications.* European Journal of Physics, 2017. **38**(3): p. 035501.
93. Sivarajah, P., et al., *What is the Brillouin zone of an anisotropic photonic crystal?* Physical Review B, 2016. **93**(5): p. 054204.

Graphical Abstract

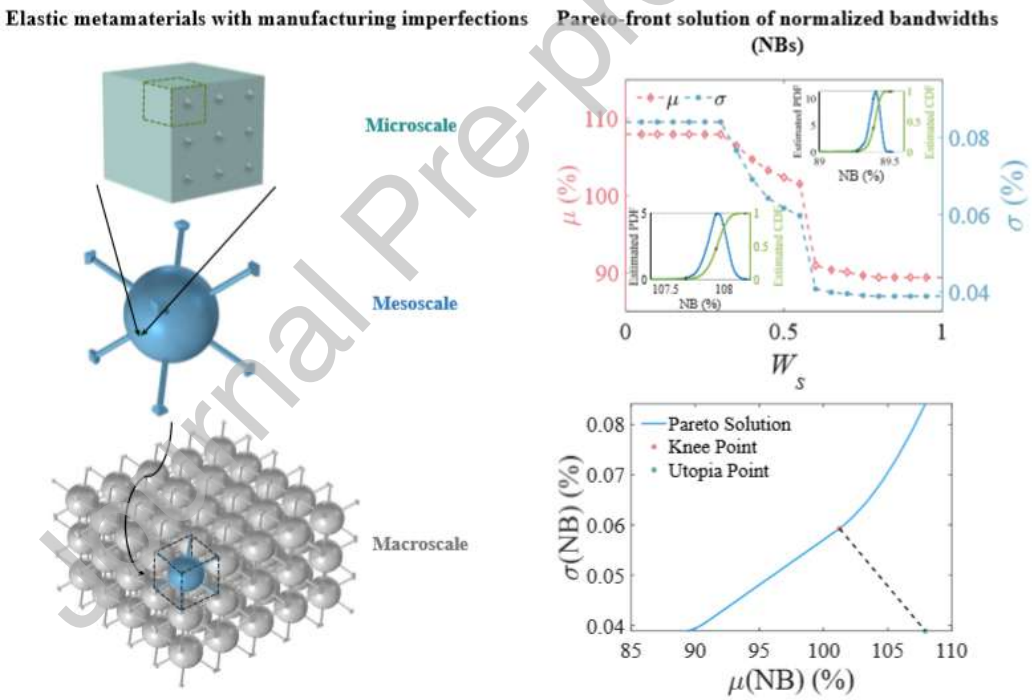

Author Contribution Statement

Minghui Zhang: Conceptualization, Software, Methodology, Validation, Formal analysis, Investigation, Writing-original draft. **Qihan Wang**: Conceptualization, Methodology, Software, Investigation, Writing-review&editing. **Zhen Luo**: Investigation, Writing-review&editing. **Wei Gao**: Supervision, Conceptualization, Funding acquisition, Writing-review&editing.

Declaration of interests

☒ The authors declare that they have no known competing financial interests or personal relationships that could have appeared to influence the work reported in this paper.

☐ The authors declare the following financial interests/personal relationships which may be considered as potential competing interests: